2020

Diffusion of Fission Products in Nuclear Graphite

Kevin Graydon
University of Central Florida

DIFFUSION OF FISSION PRODUCTS IN NUCLEAR GRAPHITE

by

KEVIN GRAYDON
B.S. University of Central Florida, 2019

A thesis submitted in partial fulfillment of the requirements
for the degree of Master of Science
in the Department of Materials Science and Engineering
in the College of Engineering and Computer Science
at the University of Central Florida
Orlando, Florida

Fall term
2020

ABSTRACT

The next generation of nuclear reactors (Generation IV) are specified to use graphite as the choice material for neutron moderation and structural components. For this reason, study of diffusion behavior of the fission product, ruthenium (Ru), in the candidate graphite grades, POCO AXF-5Q & ZXF-5Q, IG-110, NBG-18 and PCEA, is necessary. Diffusion data for Ru in these grades is absent due to the lack of prior studies and this work aims to fill this void and begin the study of this metallic fission product's diffusion behavior. By utilizing physical vapor deposition (PVD), dynamic secondary ion mass spectroscopy (SIMS), and the thin film solution to the diffusion equation coupled with a short circuit diffusion correction term, the diffusivities and Arrhenius temperature dependence are determined in the range of 500-1000°C and reported for the first time. Diffusion of Ru in this range is slow, with both lower activation energies and diffusion coefficients than other metallic fission products. Simulations of Ru diffusion on a graphene plane give activation energies similar to those acquired in this study. This is consistent with Ru behaving as an intercalating species and using the region in between graphene-like basal planes of graphite to travel through the lattice.

ACKKNOWLEDGEMENT

I want to thank Dr. Sohn and Dr. Coffey for their insight and guidance throughout the project, Mikhail Klimov for his expertise and work acquiring the depth profiles by SIMS, and Edward Dein and Quintin Cumston for their instruction and guidance on physical vapor deposition.

Finally, I want to thank Dr. Mehta for being someone I can bounce questions or ideas around with as well as my lab mates, friends, and family for their support and listening to me grumble during the more stressful times.

TABLE OF CONTENTS

LIST OF FIGURES vii

LIST OF TABLES ix

LIST OF ACRONYMS x

INTRODUCTION 1

General Background 1

Objective 2

CHAPTER 1: BACKGROUND 4

1.1 Nuclear Fission 4

1.2 Nuclear Powerplants 4

1.3 Graphite 6

1.4 The Graphite Collection 9

1.5 Secondary Ion Mass Spectroscopy (SIMS) 16

CHAPTER 2: EXPERIMENTAL METHODS 18

2.1 Sample preparation to SIMS 18

2.2 Comparison of methodology 22

CHAPTER 3: RESULTS & DISCUSSION 25

3.1 Depth Profiles 25

3.2 Fitting Method and Diffusivity Values 26

3.3 Arrhenius Relation 31

3.4 Characterization 36

3.5 Discussion 43

3.5.1 Transport Method 43

3.5.2 Variability in Calculated Diffusivities 44

3.6 Summary 48

LIST OF REFERENCES 50

LIST OF FIGURES

Figure 1. A) Cross section of a TRISO fuel particle [13]. B) The fuel compact used in the HTTR with imbedded fuel particles [14]. 6

Figure 2. Fuel block assembly from HTTR reactor [14] 7

Figure 3. Top down and side view of the graphite crystal structure respectively [18, 16] 8

Figure 4. Nuclear graphite grade: A). POCO AXF-5Q B). ZXF-5Q 10

Figure 5. Nuclear graphite grade: IG-110 11

Figure 6. Nuclear graphite grade: NBG-18 12

Figure 7. Nuclear graphite grade: PCEA 13

Figure 8. Cross-section rendering of diffusion jig assembly 20

Figure 9. AXF-5Q + Ru samples inside Phi Adept 1010 chamber for depth profiling 22

Figure 10. Post-SIMS sample. AXF-5Q annealed for 24 hours at 800°C 25

Figure 11. Full Ru/C profile for an annealed ZXF-5Q graphite sample at 1000°C 26

Figure 12. 1^{st} derivative (dots) for start and end determination 28

Figure 13. Resultant profile region 29

Figure 14. Fitted depth profile using equation 6 30

Figure 15. Diffusivity values and fitting of AXF-5Q + Ru 32

Figure 16. Diffusivity values and fitting of ZXF-5Q + Ru 32

Figure 17. Diffusivity values and fitting of IG-110 + Ru 33

Figure 18. Diffusivity values and fitting of NBG-18 + Ru 33

Figure 19. Diffusivity values and fitting of PCEA + Ru 34

Figure 20. Diffusivities modelled from Arrhenius equations 35

Figure 21. XRD of AXF-5Q + 20nm Ru film in the as-deposited and post-annealed states at 600 and 800°C 37

Figure 22. SIMS crater A) secondary electron image, B) backscattered electron image. 38

Figure 23. IG-110 + Ru annealed at 500°C, 24hrs. A). Secondary electron image of crater floor. B). Backscattered image of same area. C-E). X-ray counts of points B1-3 respectively. 40

Figure 24. IG-110 + Ru annealed at 800°C, 24hrs. A). Secondary Electron Image. B). Backscattered image of the same region. C-E). Energy spectrum of points B1-3 respectively. .. 42

Figure 25. Ru as an intercalating particle moving to neighboring or next to neighboring sites... 44

Figure 26. Ru-C phase diagram [37]..... 46

Figure 27. Film thickness by location testing, post deposition..... 48

LIST OF TABLES

Table 1. Diffusivity of Ag in various graphite grades 3

Table 2. Select properties of the nuclear graphite in this collection 14

Table 3. Manufacturing data of graphite collection [27, 24, 23] 15

Table 4. Graphite + Ru Arrhenius equations 35

Table 5. Activation energies of ruthenium in each graphite grade 44

LIST OF ACRONYMS

AG	Against Grain
BWR	Boiling Water Reactor
CPS	Counts Per Second
CTE	Coefficient of Thermal Expansion
EDS	Energy Dispersive Spectroscopy
FP	Fission Product
HTTR	High Temperature Test Reactor
PWR	Pressurized Water Reactor
SEM	Scanning Electron Microscope
SIMS	Secondary Ion Mass Spectroscopy
TRISO	Tri-structure isotropic
UCF	University of Central Florida
VHTR	Very High Temperature Reactor
WG	With Grain
XRD	X-ray Diffraction

INTRODUCTION

General Background

To aid in the design and licensing requirements for the next generation of advanced nuclear reactors, a comprehensive study of the fission products and their interaction behavior with the moderator, graphite, is necessitated. Several designs are under consideration for next generation reactors which encompass very high temperature reactors (VHTR), molten salt reactors, and fluoride salt cooled high temperature reactors. For example, VHTR designs entail a uranium fuel source with a core constructed of graphite and thermal management through helium gas cooling [1]. This work details the efforts into determining how the fission products ruthenium and silver travel through a collection of nuclear graphite consisting of AXF-5Q, ZXF-5Q, PCEA, NBG-18, and IG-110 by diffusion. This data can be used for various purposes, such as source term estimation in emergency situations [2], simulation and an increased understanding of the graphite and fission product interaction. The efforts detailed in this report are one piece of a multinational collaborative effort, sponsored by the Department of Energy Nuclear Energy University Program, into the study of the grades incorporated in the collection. The University of Central Florida team is responsible for the diffusion experimentation and analysis while our collaborators at Oak Ridge National Labs, University of Manchester, North Carolina State University and University of Loughborough perform full characterization of the grades and simulations. A litany of evaluation methodologies are enacted such as porosimetry, diffractometry, transmission electron microscopy with energy dispersive and electron energy loss spectroscopy, X-ray tomography, BET and many more.

Objective

This work aims to supply the Department of Energy with the data necessary to determine the diffusivity values of the fission products under investigation over a designated temperature range of 500-1000°C. This data can then be used for numerous forms of simulation such as codes that predict fission product release and interaction with fuel and core components to aid in the development for the next generation of nuclear power stations in the US. A detailed report on the codes and work completed in terms of fuel and fission products can be found here [3]. Diffusion of silver in nuclear graphite has not been extensively explored in the grades included in this work aside from IG-110. The diffusion behavior of ruthenium in this collection has largely not been examined. The aim of this work is to fill in this gap and begin the discussion of the diffusion of these two fission products in these grades. Table 1 below shows the previous studies of silver in different nuclear graphite. Boyle et al. [4] devised a custom cell manufactured from GR001CC graphite and reported a value of 2.385×10^{-15} $m^2 s^{-1}$ for a temperature of 1150°C. Zherdev and Platonov [5] investigated both Cs and Ag in reactor grade graphite and hypothesized diffusion was occurring by different channels, resulting in slow (5.1×10^{-12} m^2/s), intermediate (7×10^{-11} m^2/s), and fast (4×10^{-9} m^2/s) pathways of atomistic movement at 800°C. Carter et al. [6] was able to cover a range of temperatures and determine the Arrhenius relation from 775-1011°C by utilizing Inductively Coupled Plasma Mass Spectroscopy and Instrumental Neutron Activation Analysis and is reported below. In addition, The IAEA TECDOC 978 [3] gives an exhaustive listing of Ag, Cs, Sr and other fission products and their diffusion data, some of which is restated in Table 1.

Table 1. Diffusivity of Ag in various graphite grades

Graphite Grade	D (m^2/s) @ 800C	D (m^2/s) @ 1150°C	D_0 (m^2/s)	Q (eV)	Temperature range (°C)	Ref.
GR001CC	-	$2.385x10^{-15}$	-	-	1150	[4]
Reactor Grade	$4x10^{-9}$ - $5.1x10^{-12}$	-	-	-	800	[5]
IG-110	8.059E-15	-	6.60E-04	1.803	775-1011	[6]
A3-3	2.511E-17	1.829E-12	0.68	2.716	800-1300	[7]
A3-27	4.840E-16	1.779E-11	1.3	2.550	800-1300	[7]
Irradiated A3-3	4.463E-16	1.787E-11	1.6	2.570	800-1300	[7]
Matrix Graphite	9.408E-19	-	8.70E+07	4.291	800-1000	[3]

CHAPTER 1: BACKGROUND

1.1 Nuclear Fission

Nuclear fission is the process by which heat is generated due to energy release from the splitting of the U-235 atom. The U-235 isotope is unstable and when an additional neutron is introduced to the nucleus of the U-235 atom, it splits in two and releases two or three fast neutrons. The resulting atomic weights of the split atoms correspond to various elements on the periodic table and are called fission products. Two selected fission products, ruthenium and silver, are under investigation in this work. The fast neutrons travel at such a rate that impacting other U-235 atoms becomes less probable and slowing these neutrons becomes a requirement to ensure the fission process is allowed to occur without self-extinguishing [8, 9]. There are several different materials, dubbed moderators, that have been used to effectively moderate the speed of the fast neutrons. These include light water, heavy water, and graphite. Graphite was selected due its scattering and absorption cross sections of 5.551 and 0.0035 barns [10]. These parameters describe the amount of particle scatter or absorption during the elastic or inelastic interaction of the incident particles and the material [11].

1.2 Nuclear Powerplants

There are several different VHTR designs that utilize graphite as the core structural material and moderator, two of which are pebble bed and prismatic block reactors. Pebble bed reactors use spherical fuel pellets to heat He gas that either transfers heat to water to power a steam

driven turbine or the He gas powers the turbine directly [12]. Prismatic block reactors work much the same way except the core is made of interlocking prisms that contain the Uranium fuel rods. Both also double as a method of hydrogen production, adding to their versatility and commercial viability. These designs differ from the pressurized water (PWR) and boiling water reactors (BWR) currently in operation and supply approximately 20% of the electricity generated in the US [1]. They use regular (light) water as the moderating and cooling material whereas the VHTR uses graphite and gas. The Generation IV series is designed for higher output temperatures from 700°C-1000°C+ [12] which can increase the overall efficiency of power generation to nearly 48% [1]. In contrast, PWR and BWRs are about 33% efficient. VHTRs are currently in the research and development phase however similar designs with lower output temperatures have been constructed. In the late 90s and early 2000s, both China and Japan built and successfully ran a pebble bed and prismatic design reactor called the HTR-10 and High Temperature Test Reactor (HTTR) respectively [12]. These reactors serve as a test bed and research vessel for future high temperature gas reactors. The HTR-10 is helium cooled, capable of producing 10MW of thermal power and has an outlet temperature of 700°C [13]. The HTTR is also helium cooled, but capable of producing 30MW and has achieved an outlet temperature of 950°C [14]. Both use tri-structure isotropic (TRISO) fuel particles which consist of a UO_2 core coated in a layer of low density pyrolytic carbon (PyC), high density PyC, silicon carbide (SiC), and a final layer of high density PyC [13, 14, 15]. This type of configuration allows for the trapping of fission products within the particle, greater stability in terms of corrosion, oxidation resistance and irradiation effects and high temperature stability up to 1600°C [13, 15]. At temperatures above 1600°C, the SiC layer begins to fail and allow fission products (FPs) to escape. The particles used in the HTTR fuel compacts are 920μm in diameter and housed in a hollow cylinder with an OD of 26mm, ID of 10mm and

height of 39mm [14]. The HTR-10 uses a multi-layered 60mm sphere to house 8000 TRISO fuel particles, hence the name pebble bed reactor [13]. Figure 1 gives a visual representation of the TRISO fuel and the HTTR fuel compact.

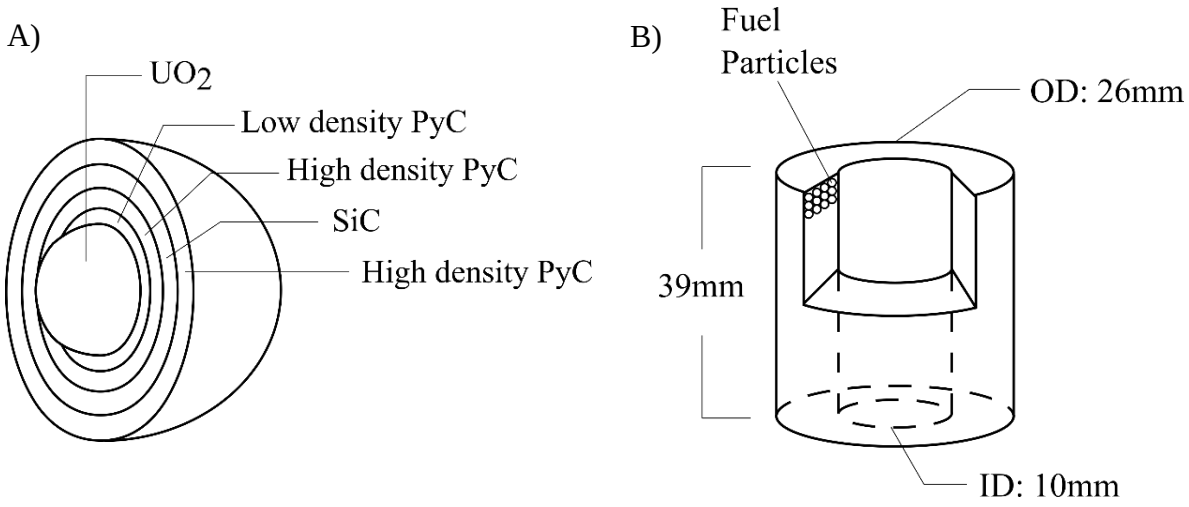

Figure 1. A) Cross section of a TRISO fuel particle [13]. B) The fuel compact used in the HTTR with imbedded fuel particles [14].

1.3 Graphite

Beyond its moderation capabilities, graphite is used in the core of the reactor due to its thermal and structural stability, isotropy, and low coefficient of thermal expansion [16]. As a result, this allows for the material to be machined into the desired geometries as dictated by the reactor designers. An example of such geometry is the HTTR fuel assembly shown in Figure 2. The holes in the top are designed for the fuel rods and dowel pins.

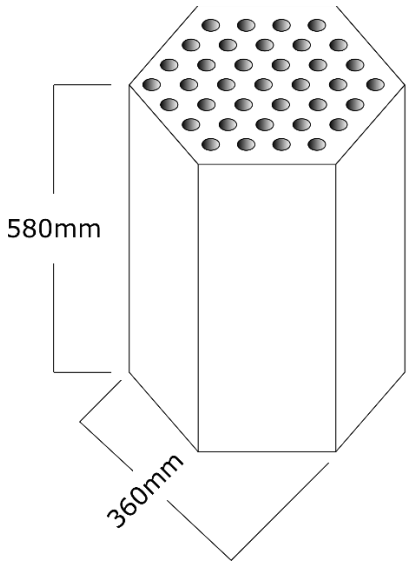

Figure 2. Fuel block assembly from HTTR reactor [14]

Graphite itself is a polycrystalline material possessing a hexagonal closed packed structure and is the more stable allotrope of carbon under normal conditions [17]. The structure is composed of successive layers of carbon atoms forming a strongly bonded honeycomb array. In contrast, these graphene-like planes are weakly held together by van der Waals bonding [18]. Figure 3 shows this structure of graphite with the distances between layers and the labelled “c” and “a” lattice parameters. In order for graphite to be successfully implemented in a reactor, it must be of high purity as the impurities increase the absorption cross-section leading to the greater absorption of neutrons [17]. Boron is a specific impurity that must be minimized as it is an effective neutron absorber. High purity graphite contains a maximum of 2ppm B whereas low purity is 10ppm according to the ASTM D7219-19 [19].

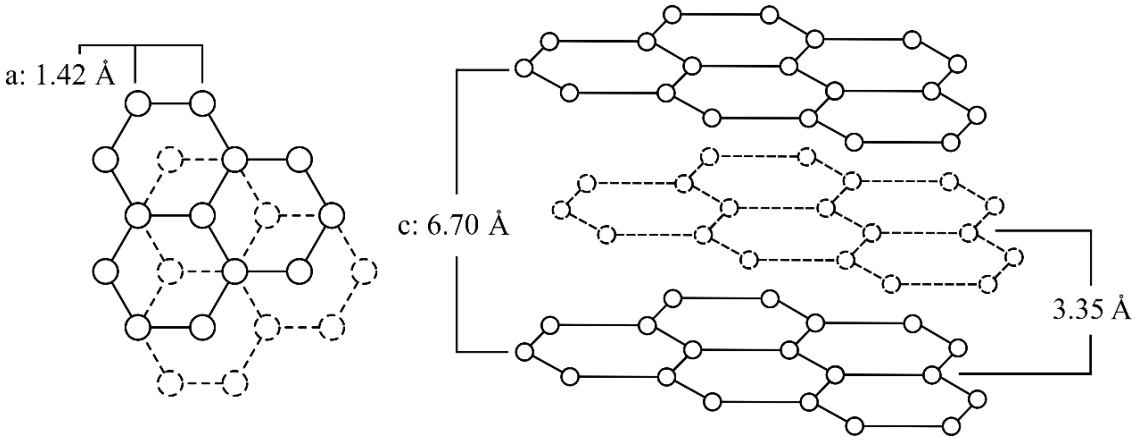

Figure 3. Top down and side view of the graphite crystal structure respectively [18, 16]

In general, the nuclear graphite used in reactors is synthetic and is manufactured from a coal tar pitch binder and petroleum or pitch coke. Coal tar pitch is the residual liquid post coal tar refinement and petroleum coke is sourced from the higher boiling point fractions in the petroleum refinement process called cracking [17, 20, 21]. The coke is responsible for the final properties of the graphite and as such, selections of coke are based on those that allow for high purity and isotropy [16]. The petroleum coke must undergo a calcination process where it is heated to 1400°C [17] for the removal of volatile hydrocarbons and consequently improves its purity. It is then crushed and sorted by size. Crushed particles possessing a diameter less than 500μm are milled to even finer diameters and form what is known as the "flour" [17]. The flour, particles, and binder are then mixed. Typically, a fifth of the mixture is binder and the remaining percentage encompasses the flour/particle combination [16]. The new product, termed "green article" is then formed through processes such as vibration molding, extrusion, and isostatic pressing. Following formation, the solid is baked at 800°C [16] for up to several days, impregnated with pitch and baked again. The "baked article" is now subjected to the graphitization process in which a large

current is passed through the structure to raise it to a temperature of approximately 2800°C. This process can last several days [16]. The result is the high-purity graphite. This is the general process, but different manufacturers have specialized and/or proprietary process variations for additional refinements such as enhanced purification and grain size control.

1.4 The Graphite Collection

In this work, the interaction of various fission products in a collection of nuclear grade graphite is under investigation. The goal is to determine the diffusivity of two fission products, ruthenium and silver, in the AXF-5Q, ZXF-5Q, IG-110, NBG-18 and PCEA graphite grades. Table 2 gives various properties for the grades in question. For reactor use, the graphite must be isotropic or near-isotropic as defined by the ASTM D7219 standard. Taking the ratio of the coefficient of thermal expansion (CTE) in the against grain (AG) and with grain (WG) directions gives the degree of anisotropy. AG describes preferential crystallographic alignment for the filler particles along the c-axis and WG describes that along the a-axis [16, 22]. The difference in properties can be influenced by the manufacturing method. Methods such as extrusion can result in properties varying the CTE if samples are taken perpendicular (AG) or parallel (WG) to the extrusion direction [22, 23]. Values of the CTE ratio between 1 and 1.1 for molded, isomolded and extruded are deemed isotropic and graphite with ratio values ranging from 1.1-1.15 are labeled as near-isotropic [19]. Table 2 makes note of this in the reported property values and Table 3 summarizes the coke type, manufacturing method and maker of each graphite.

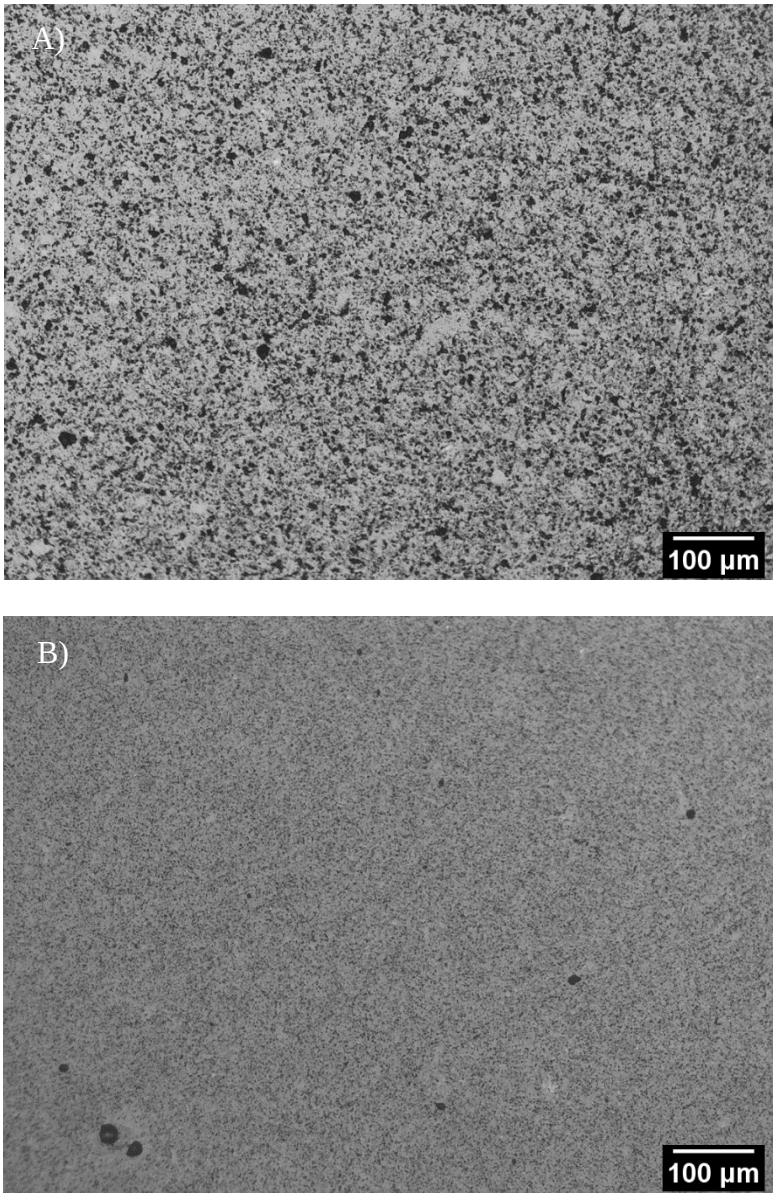

Figure 4. Nuclear graphite grade: A). POCO AXF-5Q B). ZXF-5Q

The POCO grades AXF-5Q and ZXF-5Q are ultrafine and microfine grades respectively based on their grain size as per the ASTM D7219-19 standard [19]. They are isotropic grades that are reportedly formed by isostatic pressing [24] but their manufacturing process is proprietary and largely unreported in literature. Figure 4A and B show micrographs of the polished surface before

thin film deposition of the FP. The dark regions highlight the fine pore size of the two grades. This is in direct contrast to the much larger size of the pores seen in the other grades in the collection below. They are both being studied for possible use in the next generation of reactors but are not currently found in any reactor.

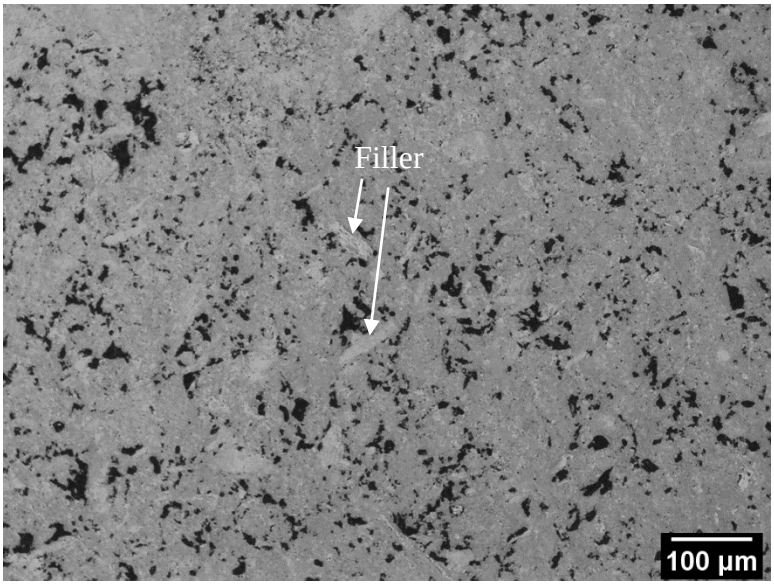

Figure 5. Nuclear graphite grade: IG-110

IG-110 is a nearly isotropic, superfine graphite based on a petroleum coke and formed by iso-molding [25]. It is the only grade in this collection currently in use in a power station and is used in Japan's High Temperature Test Reactor and China's HTR-10 as structural materials and reflectors. Figure 5 shows a micrograph of a polished IG-110 sample. With petroleum cokes, needle-like structures form due to grain alignment during the calcination process of manufacturing [26]. While the overall structure behaves isotropically, these needle-like structures behave anisotropically and are labeled in the same micrograph above. By way of visual comparison, the

POCO grades contain much finer pores than those found in IG-110 while the two maintain similar porosity values of 20% to 22% respectively [27, 25].

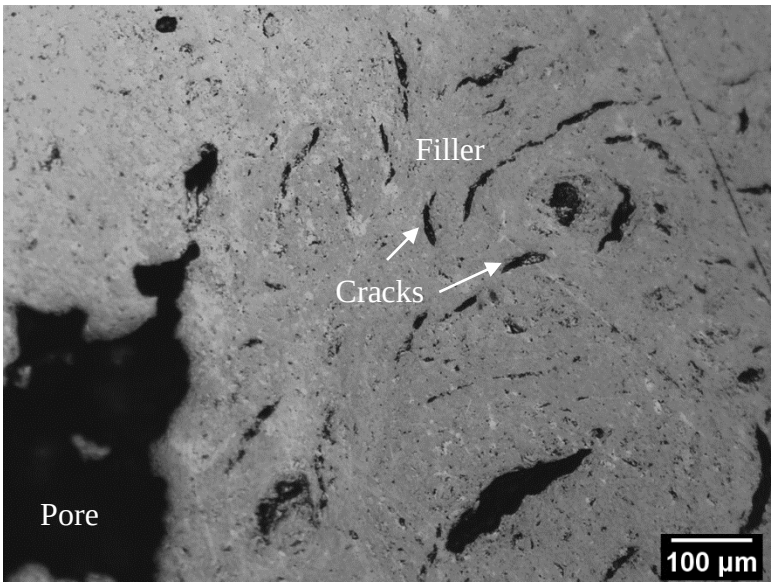

Figure 6. Nuclear graphite grade: NBG-18

NBG-18 is a medium grained graphite formed with a pitch-based coke and manufactured by vibration molding. This grade is under consideration for the core regions of pebble bed reactors and neutron reflectors [28]. It can be seen from Figure 6 that NBG-18 contains a range of pore sizes and larger than those found in the previously mentioned grades yet contains 18.3% porosity. The filler particles, labeled above, take on a circular shape when sectioned and is associated with reduced alignment of crystallites in the matrix and consequently results in isotropy of the particle [26]. The long cracks seen within the filler particle region are the result of shrinkage due to the calcination process [26] during formation.

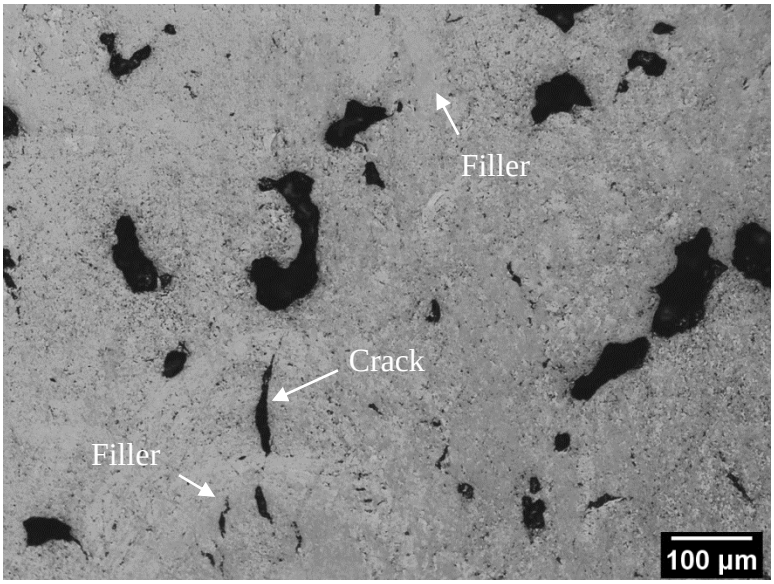

Figure 7. Nuclear graphite grade: PCEA

PCEA is the final graphite in this collection. It is a medium grained, petroleum-based graphite that is formed by extrusion. PCEA is composed of both acicular and spherical particles with Kane et. al. [26] reporting as much as 70% possess the needle-like form. Similar shrinkage cracking and spherical filler particles are seen in Figure 7 as with NBG-18. The grade is under consideration for both pebble bed and prismatic reactor designs. Its potential role in the pebble bed reactor is to serve as a reflector or insulation pieces whereas it will serve as a fuel element in the prismatic reactor [28].

Table 2. Select properties of the nuclear graphite in this collection

Property	AXF-5Q [27, 19]	ZXF-5Q [27, 19]	IG-110 [25, 19]	PCEA	NBG-18
Grain size (μm)	Ultrafine | 5	Microfine | 1	Superfine | 20	Medium | <800 [25, 19]	Medium | <1600 [29, 19]
Density (g/cm^3)	1.78	1.78	1.77	1.84 [26]	1.85 [25]
Porosity by volume	20%	20%	22.7% [25]	-	18.3 [25]
Compressive (MPa)	156	175	73.4 / 69.6*	-	80 [29]
Tensile (MPa)	62	79	24.9 / 24*	23.5 / 21.6 [25]*	20 [29]
CTE	7.9 μm/m°C	8.1 μm/m°C	4E-6 / 3.6E-6 (K^{-1})*	3.5E-6 / 3.71E-6 (K^{-1}) [24]*	4.5E-6 / 4.6E-6 (K^{-1}) [29]*
Isotropic ratio (AG/WG)	1	1	0.9	1.06	1.02
Thermal Conductivity (W/mK)	95	70	124 / 138*	143 / 146 [25]*	140 [29]

*Designates values in the reported with grain (WG) / against grain (AG) directions respectively

Table 3. Manufacturing data of graphite collection [28, 25, 24]

	AXF-5Q	ZXF-5Q	IG-110	PCEA	NBG-18
Coke	-	-	Petroleum	Petroleum	Pitch
Manufacturing Method	Isostatic Pressing	Isostatic Pressing	Iso-molding	Extrusion	Vibration molding
Manufacturer	POCO	POCO	Toyo-Tanso	GrafTech	SGL

1.5 Secondary Ion Mass Spectroscopy (SIMS)

The idea of SIMS was introduced in 1949 by Herzog and Viehboeck with a demonstration of depth profiling by SIMS occurring in 1958 by Honig. Liebl made the debut of commercially available systems nine years later [30]. The technique has been adopted and heavily implemented in the semiconductor industry as well as the study of surfaces and interfaces.

Secondary ion mass spectroscopy is a sensitive surface analysis technique that uses an ion source to bombard the surface of a sample with primary ions [31, 32]. There are two types of SIMS: static and dynamic. Static SIMS is a surface level analysis technique whereas dynamic SIMS can dwell further beyond the surface on the order of microns.

As a result of the impact from primary ions on the sample surface and subsurface, energy transfer occurs from the primary ions to the atoms residing above and below the initial surface layer. The resulting displacement of atoms due to this energy transfer is known as the collision cascade [30, 31]. If enough energy is transferred, atoms are ejected which is the fundamental process of sputtering. The ejected particles originate from the initial atomic surface layers or about 0.3-0.5nm from the impinged surface [31]. Sputtered particles, known as secondary particles, can take the form of positive or negative ions, neutrals, mono and polyatomics, as well as resputtered primary ions [31]. Despite the size of the collision cascade, only a small number of particles are actually sputtered from the surface as they are in the appropriate spatial location and contain the right amount of energy to be ejected.

Ejected particles that have a net charge (ions) are channeled into a mass spectrometer via electric or magnetic fields and then analyzed based on the incoming particles' mass/charge ratio.

This can give errors as two different species can have the same or nearly the same mass and be counted as one or the other if the detector does not possess adequate resolution. Additional errors can occur if particles are collected over the entire raster area. In dynamic SIMS, the sputtering erodes the surface over the raster area of the beam creating a mostly flat-bottomed crater. Particles are generally collected from some ratio of the raster area to avoid sidewall effects. Sidewall effects occur when the removed particles originate from different depths along the crater wall, giving an inaccurate representation of the material at the current dwell depth.

The acquired data is plotted on an intensity or counts per second graph against sputtered time. Crater depths and ion beam current are used calculate the dwell rate of the process. While the profile is not a 1:1 description of the concentration within the profiled specimen, it is an accurate representation of the level of relative abundance of a certain atomic species within the sample in question [32].

CHAPTER 2: EXPERIMENTAL METHODS

2.1 Sample preparation to SIMS

Graphite samples are first sectioned from the bulk, as received, blocks of material. Grades in the test collection are ZXF-5Q, AXF-5Q, IG-110, NBG-18 and PCEA. Physical sample size is typically 7x7x3mm as this size allows for many samples to be prepared from the bulk, in addition to fitting in the diffusion jigs needed to hold the sample in place during the anneal. Samples have a flat surface from machining or are made as flat as possible by hand. Encasing in epoxy was attempted as the dimensions allow for usage of a mechanical, motorized polishing machine and would provide a flat, final surface. However, due to the porous nature of graphite, the epoxy was found to infiltrate the sample even after attempting to seal off the body before encasing. Epoxy in the sample is an unwanted impurity. This resulted in a change in the preparation algorithm to hand polishing as there is a lower risk of sample contamination. Samples are polished by hand up to 1μm resulting in a mirror-like finish.

Polished samples are taken to a clean room to receive a thin film of the fission product under investigation. Samples are placed on a holding substrate and inserted into an AJA International, multi-gun, load locked, sputter deposition system. Utilizing the necessary elemental target of the FP and knowing the deposition rate at 4mTorr Ar and 200W, a film of appropriate thickness is deposited. In this work, 20nm of Ru and 30nm of Ag are deposited to form diffusion samples. Film thicknesses are confirmed by a blank piece of sapphire accompanying the deposit and then subject to X-ray reflectivity analysis. The thickness confirmation process is identical for Ag but an adhesion layer of Ti on the sapphire is needed to enhance Ag ability to bond to the

sample so the deposited thickness can be determined. The Ti layer is included for the deposition rate test only, Ti is not deposited on the graphite samples.

Optical micrographs of the specimens are then taken using a Nikon Metaphot with Motic 10MP Camera attachment. To ensure a representative set of images of the surface are acquired, samples are imaged at 10X magnification in a pattern replicating that of the 5^{th} face on a 6-sided die. Images from the center and four corners are taken before and after annealing for visual comparison.

The diffusion couple assembly consists of a piece of single crystal sapphire placed above and below the graphite sample. Stainless steel pucks are then placed above and below the sapphire pieces and fastened together to hold the assembly. A cross sectional view of the jig assembly is shown in Figure 8 below. The sapphire pieces act as a diffusion barrier between the fission product and the stainless steel. The assembly is then inserted and sealed in a high purity GE 214 quartz tube. Inside the same tube, a piece of tantalum foil, 0.025mm thick and 99.95% purity, is placed as an indicator for excessive oxidation. Tantalum readily oxidizes and should it be found to have crumbled after the anneal, it indicates oxygen was able to penetrate the tube due to poor encapsulation and negatively affect the sample. In addition, powdered graphite of the same grade is placed inside as well. This ensures the vapor pressure of carbon is in equilibrium in vacuum and decreases the likelihood that the graphite sample will vaporize.

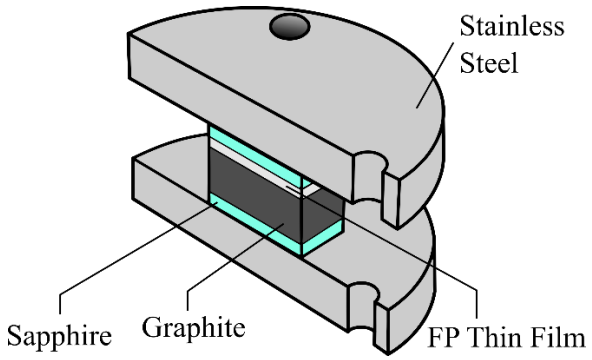

Figure 8. Cross-section rendering of diffusion jig assembly

The tube and contents are lightly heated to promote outgassing of the materials while repeatedly pumped down to roughly 1 torr and backfilled with ultra-high purity Ar. In the final stage, it is pumped down to 10^{-6} Torr and then subsequently backfilled with ultra-high purity Ar to an appropriate pressure to equate to atmospheric conditions at the desired anneal temperature. Equation 1 is used to determine the correct internal pressure by utilizing a combination of Charles' and Boyles Law for ideal gases. T_1 is the absolute temperature of the tube at time of backfilling, P_2 is 760 Torr, T_2 is the annealing temperature in Kelvin, and the backfilled pressure, P_1, can be solved for. Backfilling the quartz tube to achieve 760 torr at the anneal temperature is necessary as too high or low of a pressure could cause the tube to fail, allowing for oxygen ingress and forfeiture the sample.

$$\frac{P_1}{T_1} = \frac{P_2}{T_2} \tag{1}$$

For the temperature range of 500-1000°C, a Lindberg/Blue M Tube Furnace was used. The tube is inserted into the furnace and once the desired time has elapsed, 24 hours in this work, it is

removed and allowed to air cool outside of the furnace. Once cooled, the tube is carefully opened, and the contents inspected. The condition of the tantalum foil is checked to ensure the experimental sample is still viable and the specimen is removed. The sample surface is then once again imaged, ideally taking images at the same location as before the anneal. This is not always a viable option due to some grades having very fine features not easily distinguishable from location to location on the sample. In this case, a representative image of the area is taken.

After cooling and image collection, depth profiles are acquired by SIMS on a Phi Adept 1010 Dynamic SIMS system. A Cs^+ beam is utilized instead of an oxygen beam as the ions available are heavier and allow for better sputtering against the metallic fission products. An oxygen beam was initially tried but it was found that the oxygen ions were incapable of sputtering the ruthenium ions effectively while reactively milling the graphite and pushing the ruthenium deeper into the sample. The raster is conducted over an area of 600x600μm and sampling of the inner 120x120μm area is done to minimize the artifacts incurred by the sidewall effects. A minimum of 2 areas, the center and a corner, receive sputtering treatment. This is used as a check for uniform diffusion and statistical confidence in the back calculated diffusivity values. The depth of the sputtered area depends on the grade, anneal temperature, and fission product but ranges from several hundred nanometers to 1.5μm. Figure 9 shows several AXF-5Q + Ru samples undergoing depth profiling via SIMS. Upon completion, contact profilometry is done to determine crater depth and is correlated back to sputtering rate.

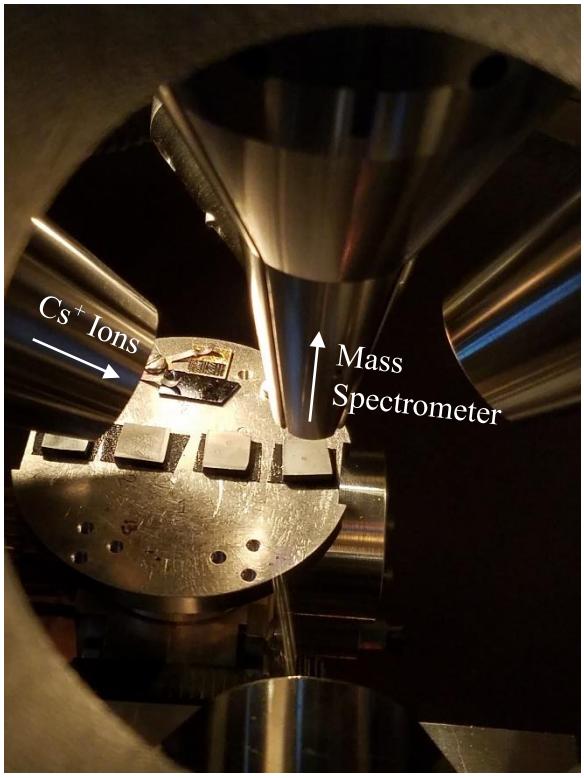

Figure 9. AXF-5Q + Ru samples inside Phi Adept 1010 chamber for depth profiling

2.2 Comparison of methodology

The experimental methods described here differ from those implemented by the various authors found in Table 1. In the case of Ag diffusion in graphite at 800°C, the diffusivity can be seen to span seven orders of magnitude and highlights the variability in the found data. With the diffusivity potentially being affected by the pore network, impurities, radiation damage etc. [6], the variability between grades may be evident due to the graphite characteristics. However, the authors used variations of the release method and the sectioning method to determine the diffusivity values. The release methods used incorporate the impregnation of a graphite sample with the radioisotope Ag which is then brought to temperature. The Ag is released from the sample

via vaporization and diffusion data is acquired by either capturing the vaporized metal on a series of targets that are later sectioned [7] or by mass spectrometer [6]. The sectioning method captures the relative activity of a radioisotope by thin layer removal [5]. While the release method used in those studies allow for a diffusivity to be found, it may be capturing the activation energies of the multiple processes that occur. For example, the Ag must first diffuse through the sample then vaporize, both of which require some amount of energy to allow for atom movement and phase change. The sectioning method works well if equipment such as lathes and microtomes are available to remove thin slices of the sample. This method is viable if the diffusivity is greater than 10^{-18} m^2/s to allow for a suitable diffusion length [33] and for slices of appropriate thickness to be removed. Diffusivities smaller than 10^{-18} m^2/s require different methods to be used.

The methodology discussed and utilized in this work contrasts those of the other authors by implementing a more simplistic but direct approach. The diffusion process is better isolated as it is mainly driven by the concentration gradient that exists between the Ru film and C and the anneal temperature. The collection of the FP by vaporization as found in previous studies is not necessary in this experimentation methodology and vaporization is one less phenomenon included in the determined diffusivity value and ultimately activation energy. The addition of the sapphire diffusion barrier in the half-sandwich setup helps ensure 1D motion of the atoms into the graphite. The physical sample size and simple geometry allow for a film to be deposited on numerous samples at once thereby minimizing run to run variability of the Ru layer. Finally, depth profiling with SIMS allows for profiles to be acquired in a smaller window of time and can be used to find smaller diffusivity values than the sectioning method allows. Values as low as 10^{-23} m^2/s [33] can be found using sputtering methods compared to 10^{-18} m^2/s by sectioning. These processes together

lend itself to a method for conveyor belt experimentation and a wider range of diffusivity determination.

CHAPTER 3: RESULTS & DISCUSSION

3.1 Depth Profiles

Depth profiles were acquired by SIMS using a 6 keV Cs^+ beam and a current of 200nA. A minimum of two spots were selected, one in the center and corner, and can be seen in Figure 10 below.

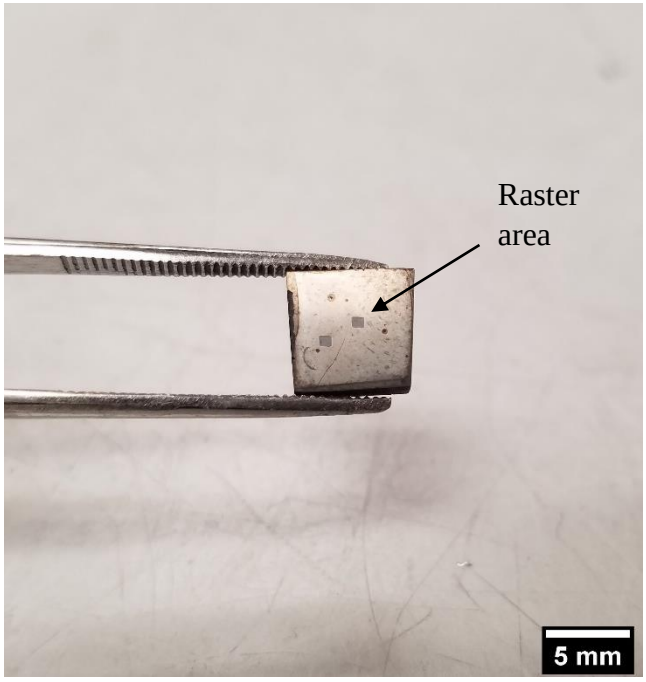

Figure 10. Post-SIMS sample. AXF-5Q annealed for 24 hours at 800°C

The ratio of Ru and C ion counts per second (CPS) is plotted to normalize the ruthenium signal to the carbon signal. This is done to mathematically cancel the instrumental errors introduced during collection. The full depth profile of a corner raster on log scale of the ion counts

ratio versus depth for a ZXF-5Q sample annealed at 1000°C with a thin film of Ru is plotted in Figure 11. In order to determine a diffusivity value from the profiles, a standard data processing procedure was developed and applied to all data sets. It is important to note that in this sample, noise induced fluctuations in the signal begin in the 1E-3-1E-4 range and signals beyond are therefore not considered for the diffusion analysis due to the uncertainties incurred**.**

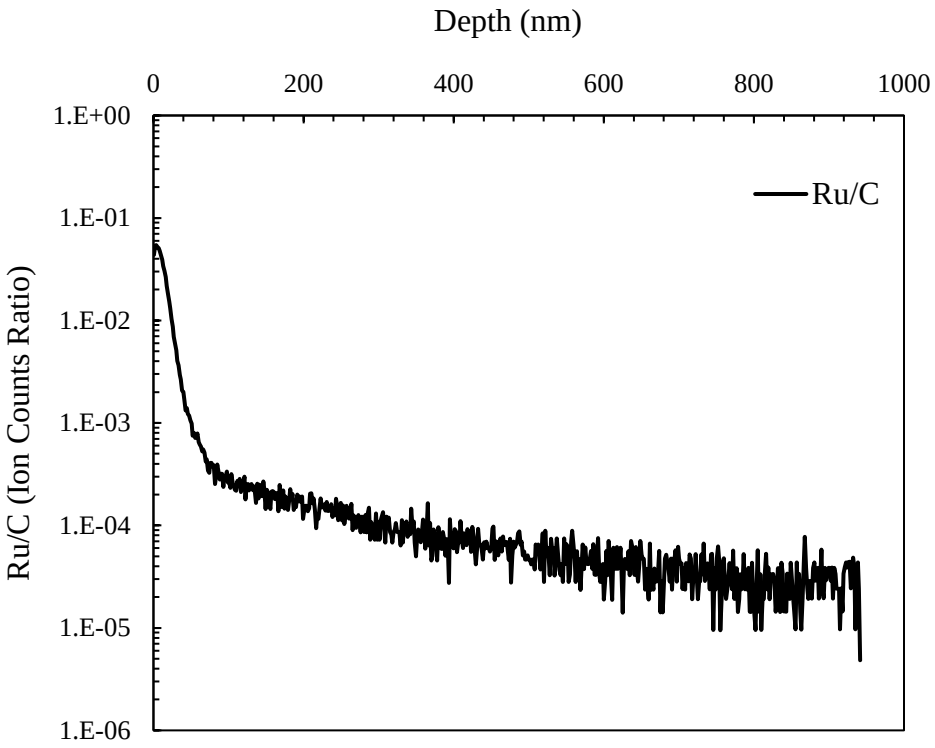

Figure 11. Full Ru/C profile for an annealed ZXF-5Q graphite sample at 1000°C

3.2 Fitting Method and Diffusivity Values

With the depth profiles received from SIMS, the decaying curve shows the trend of the gradual reduction in FP atoms detected as a function of depth. The Gaussian thin film solution in

equation 2 below allows for a one-dimensional diffusion analysis to be performed on the depth profiles to extract a diffusivity value. M is the area normalized particle count, D is the diffusivity (m^2/s), t is time in seconds, and x is the depth. The FP is deposited on the planar face of the grade in question at t = 0 and the concentration of the FP in the bulk graphite sample at this time is zero. At times t > 0, motion of the diffusant occurs and results in a nonzero concentration over the depth the atoms traverse in an allotted period of time.

$$C(x,t) = \frac{M}{\sqrt{\pi D t}} \exp\left(\frac{-x^2}{4Dt}\right) \text{ [33]} \quad (2)$$

Equation 2 is transformed into the following for fitting:

$$C(x,t) = A \exp\left(-\frac{x^2}{B}\right) \quad (3)$$

In order to have a systematic method of determining the start and end points for fitting, the first derivative of the Ru/C ratio is taken. The minimum defines the inflection point of the curve and is chosen as the start to omit any initial surface effects from the sputtering. The end point is chosen based on where the derivative nearly goes to zero. Figure 12 shows the derivative alongside the original data.

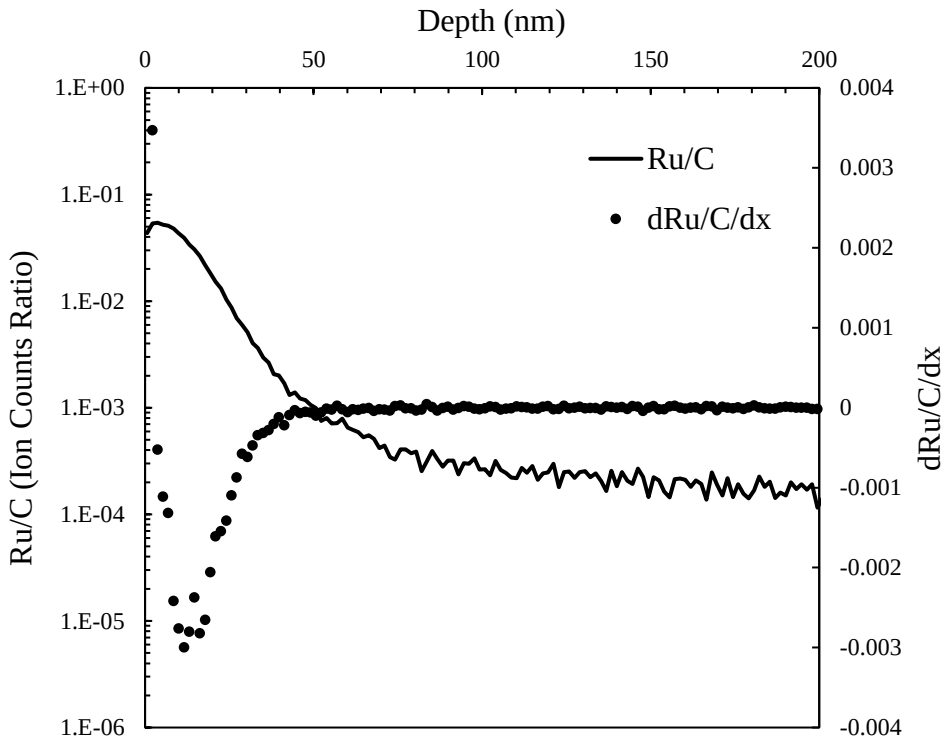

Figure 12. 1st derivative (dots) for start and end determination

The resulting profile section is truncated and the results of which are shown in Figure 13. The profile exhibits non-gaussian behavior and is not completely described when fitted with equation 3. The tail of the profile does not lay flat and is indicative of potential "short circuit" or grain boundary diffusion occurring within the matrix. A second equation, equation 4, is introduced to account for the observed non-gaussian behavior. Grain boundary density is related to the "C_0" coefficient and lattice and grain boundary diffusivity is intertwined in the "A" coefficient [33]. Appending equation 4 with 2 yields the new thin film diffusion solutions with a grain boundary diffusion correction factor. Furthermore, the updated equation for profile fitting is found in equation 6 where E and F are the additional fitting parameters.

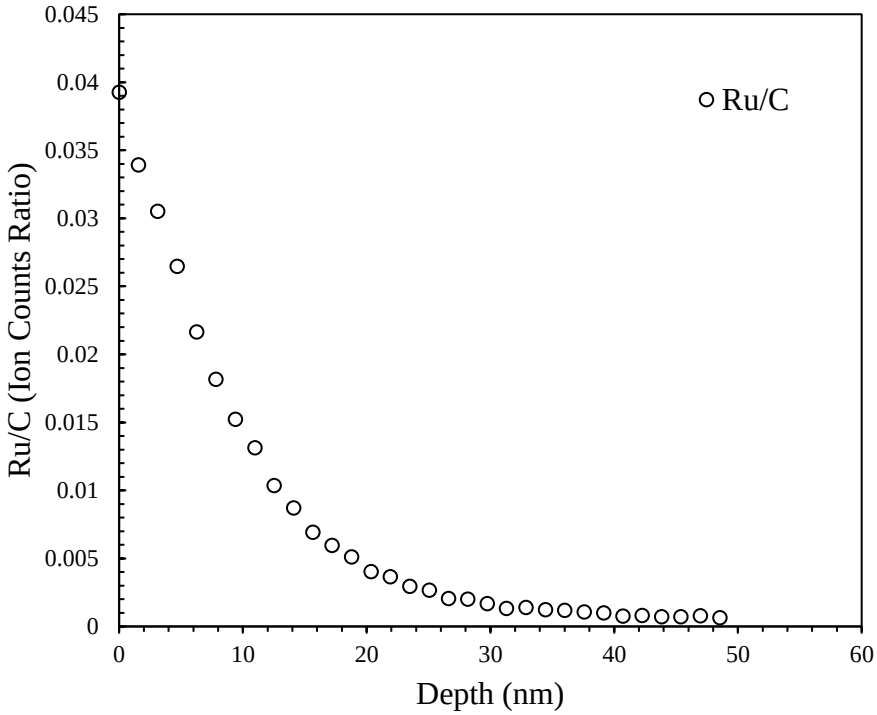

Figure 13. Resultant profile region

$$\text{Short circuit correction factor} = C_0 \exp\left(-A\, x^{\frac{6}{5}}\right) \text{ [33]} \tag{4}$$

$$C(x,t) = \frac{M}{\sqrt{\pi D t}} \exp\left(\frac{-x^2}{4Dt}\right) + C_0 \exp\left(-A\, x^{\frac{6}{5}}\right) \text{ [33]} \tag{5}$$

$$C(x,t) = A \exp\left(\frac{-x^2}{B}\right) + E \exp\left(-F\, x^{\frac{6}{5}}\right) \tag{6}$$

Fitting is achieved through the Sum of Squared Errors (SSE) method as found in equation 7. The difference between the SIMS data and the value predicted by the model, y_i and $\hat{y}_i$ respectively, are squared and summed. Variables A, B, E, and F are manipulated until the sum of the square of the errors reaches a minimum value. At this point the model has reached its best fit. The GRG nonlinear solving method in the Excel Solver function is used to numerically solve for the minimum by changing the fitting variables. Fitting the mathematical model in equation 6 to the profile in Figure 13 yields the fit shown in Figure 14 and a diffusivity value of 1.4E-20 m^2/s for Ru diffused into ZXF-5Q at 1000°C for 24 hours. This fitting algorithm is applied for all depth profiles acquired through SIMS.

$$\mathrm{SSE} = \sum[y_i - \hat{y}_i]^2 \text{ [34]} \tag{7}$$

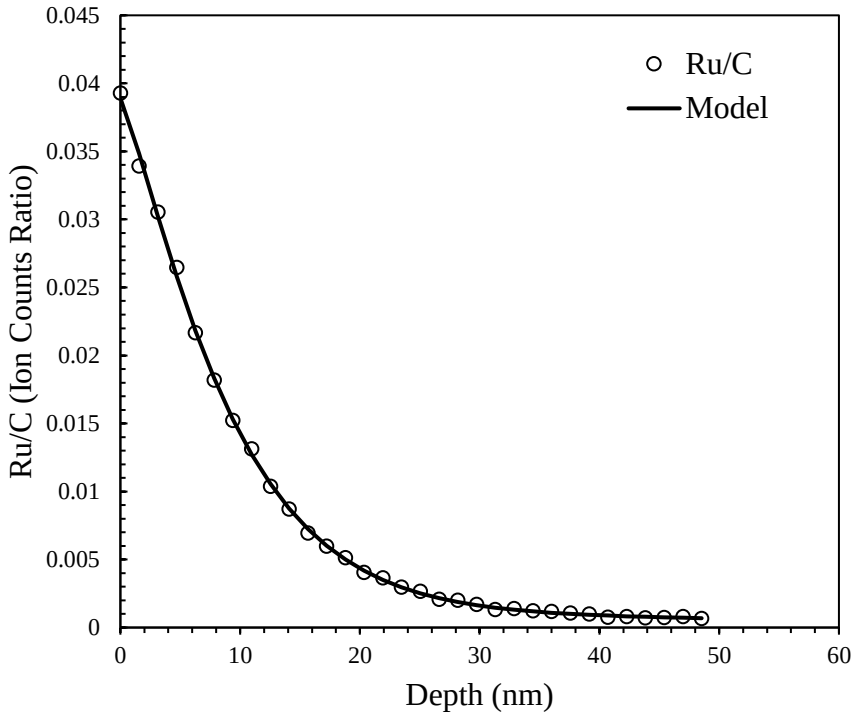

Figure 14. Fitted depth profile using equation 6

3.3 Arrhenius Relation

The diffusion of a species through a matrix possesses a dependency on temperature, where higher temperatures equate to enhanced diffusion. This dependence can be modeled through the Arrhenius relation. Equation 8 allows for the diffusivity to be calculated at any temperature along a specified range with a known activation energy, Q (J), and diffusion coefficient, D_0 (m^2/s), where T is the absolute temperature and R is the gas constant. Activation energies and diffusion coefficients are determined by linearizing equation 8 into 9 and performing a subsequent regression analysis on the diffusion values. The natural log of the experimental diffusion values is plotted against the reciprocal of absolute temperature to obtain the slope which holds activation energy information. Figure 15Figure 19 show the accumulated diffusivity values and their linearly fitted counterparts. Due to the spread in the diffusivity data, the Arrhenius relation will under and overpredict select diffusivity values. Diffusivities for silver in this temperature range were not available at time of writing due to unforeseen experimental challenges.

$$D = D_0 \exp\left(\frac{-Q}{RT}\right) \text{ [33]} \tag{8}$$

$$\ln D = -\frac{Q}{R}\left(\frac{1}{T}\right) + \ln D_0 \tag{9}$$

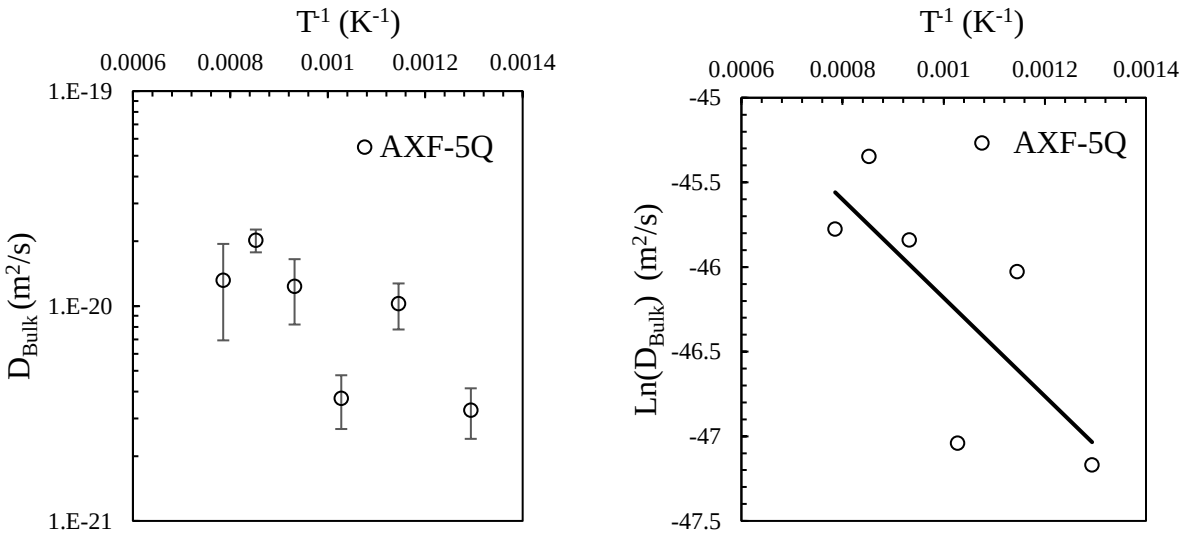

Figure 15. Diffusivity values and fitting of AXF-5Q + Ru

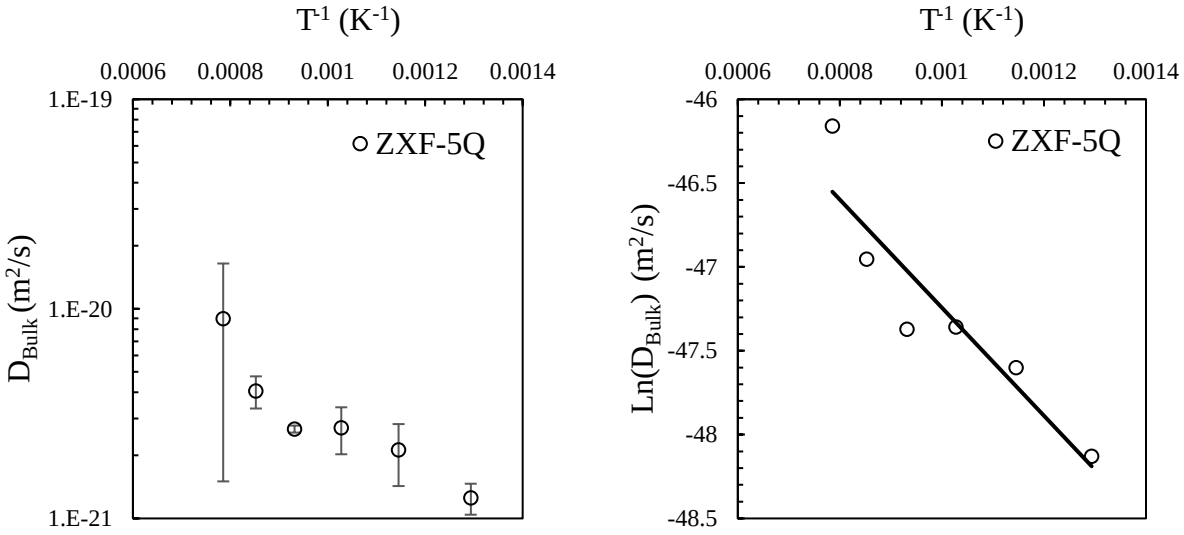

Figure 16. Diffusivity values and fitting of ZXF-5Q + Ru

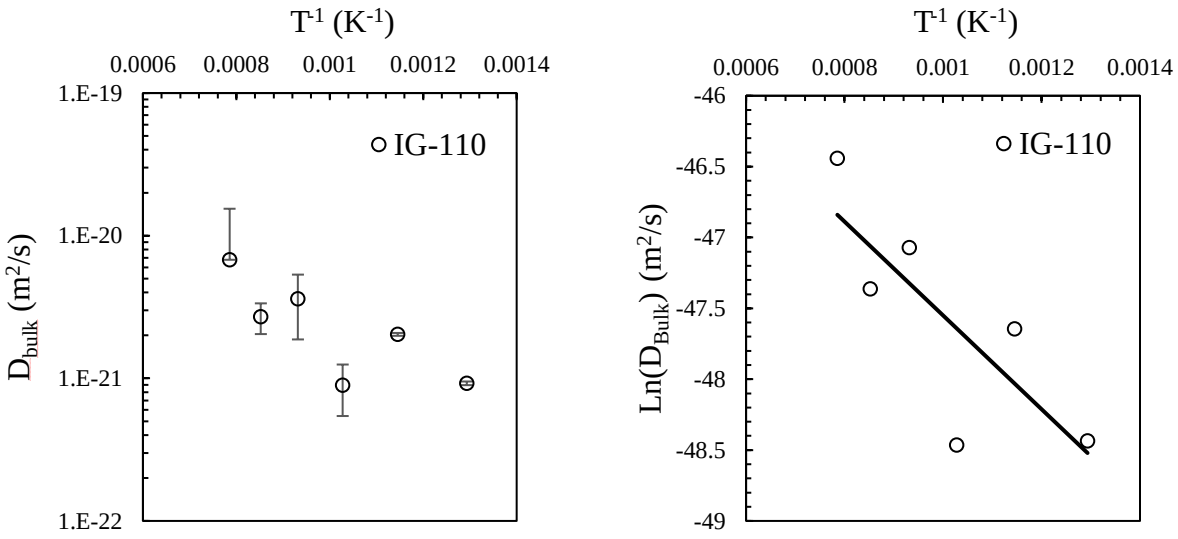

Figure 17. Diffusivity values and fitting of IG-110 + Ru

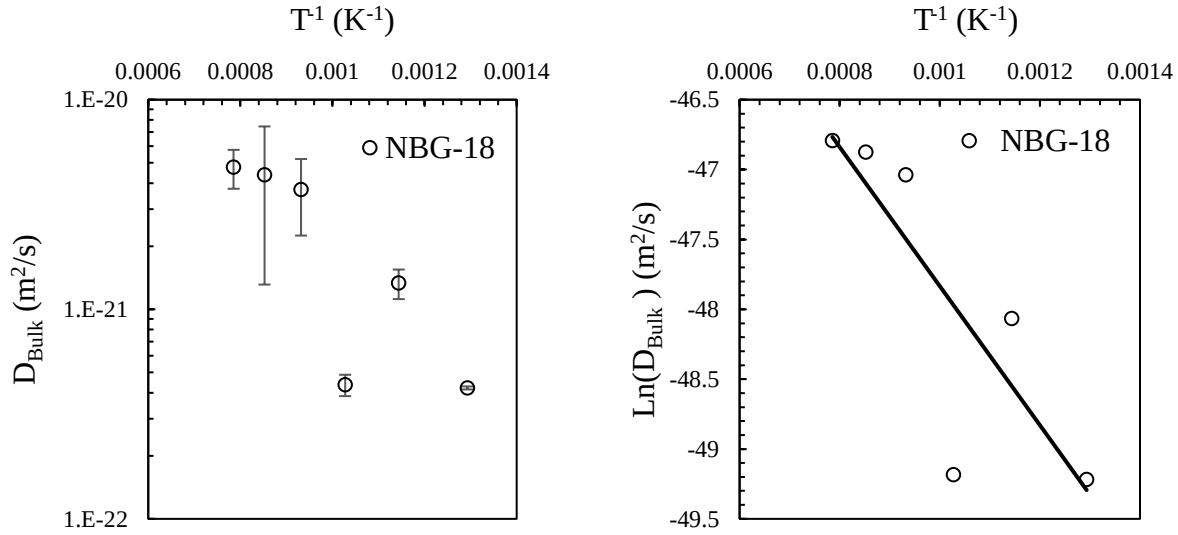

Figure 18. Diffusivity values and fitting of NBG-18 + Ru

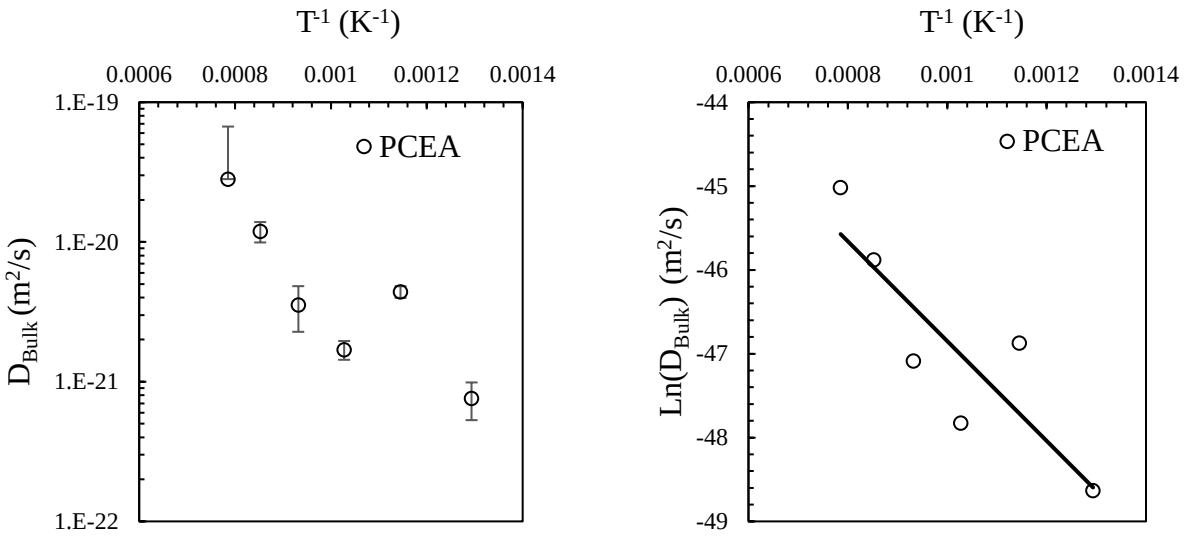

Figure 19. Diffusivity values and fitting of PCEA + Ru

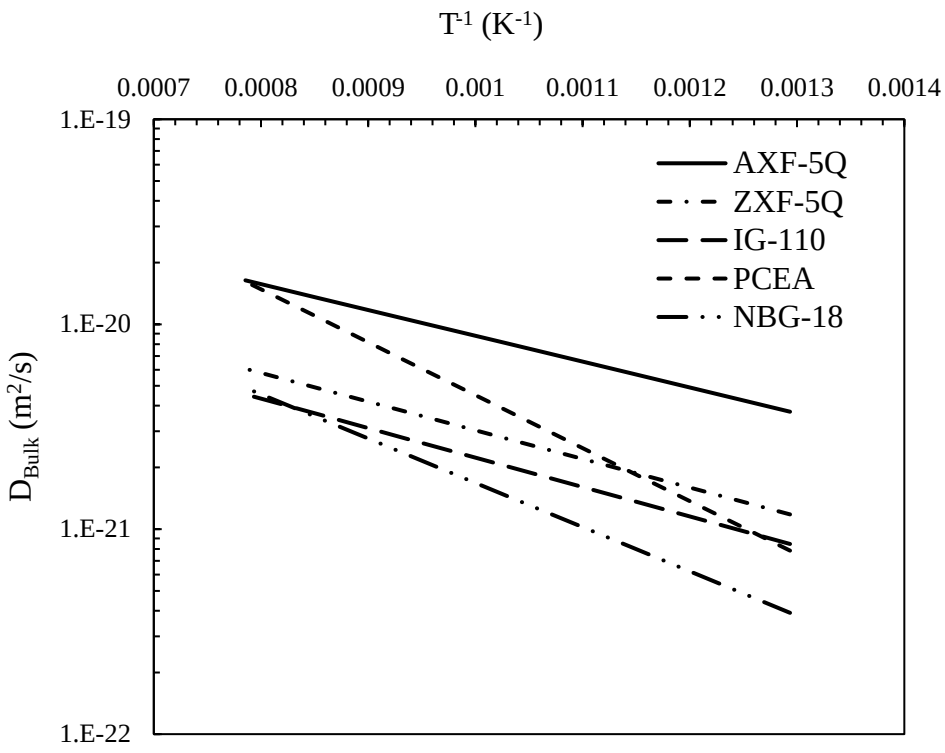

Figure 20. Diffusivities modelled from Arrhenius equations

Table 4. Graphite + Ru Arrhenius equations

Graphite Grade	D (m^2/s, 500-1000°C)
AXF-5Q	$1.60\text{x}10^{-19}\exp\left(-\frac{24.19\text{kJ}}{\text{RT}}\right)$
ZXF-5Q	$7.61\text{x}10^{-20}\exp\left(-\frac{26.79\text{kJ}}{\text{RT}}\right)$
IG-110	$6.11\text{x}10^{-20}\exp\left(-\frac{27.51\text{kJ}}{\text{RT}}\right)$
NBG-18	$2.43\text{x}10^{-19}\exp\left(-\frac{41.36\text{kJ}}{\text{RT}}\right)$
PCEA	$1.72\text{x}10^{-18}\exp\left(-\frac{49.46\text{kJ}}{\text{RT}}\right)$

3.4 Characterization

Due to the collaborative nature of this project and the roles of the collaborators at other sites to provide characterization of the graphite samples, an extensive characterization of the as-deposited and annealed samples was not carried out at UCF. However, some initial characterization work was done in attempt to see if the variability in the data could be explained by bulk microstructural changes. X-ray diffraction (XRD) was carried out using a PANalytical Empyrean with a Cu source with Kα wavelength of 1.540598 nm. AXF-5Q graphite with a 20nm Ru film in the as-deposited, 600°C and 800°C annealed states were chosen for investigation due to their availability at time of testing. The diffraction of the annealed states compared to the as-deposited states (Figure 21) immediately suggests no obvious crystallographic change has occurred due to the annealing.

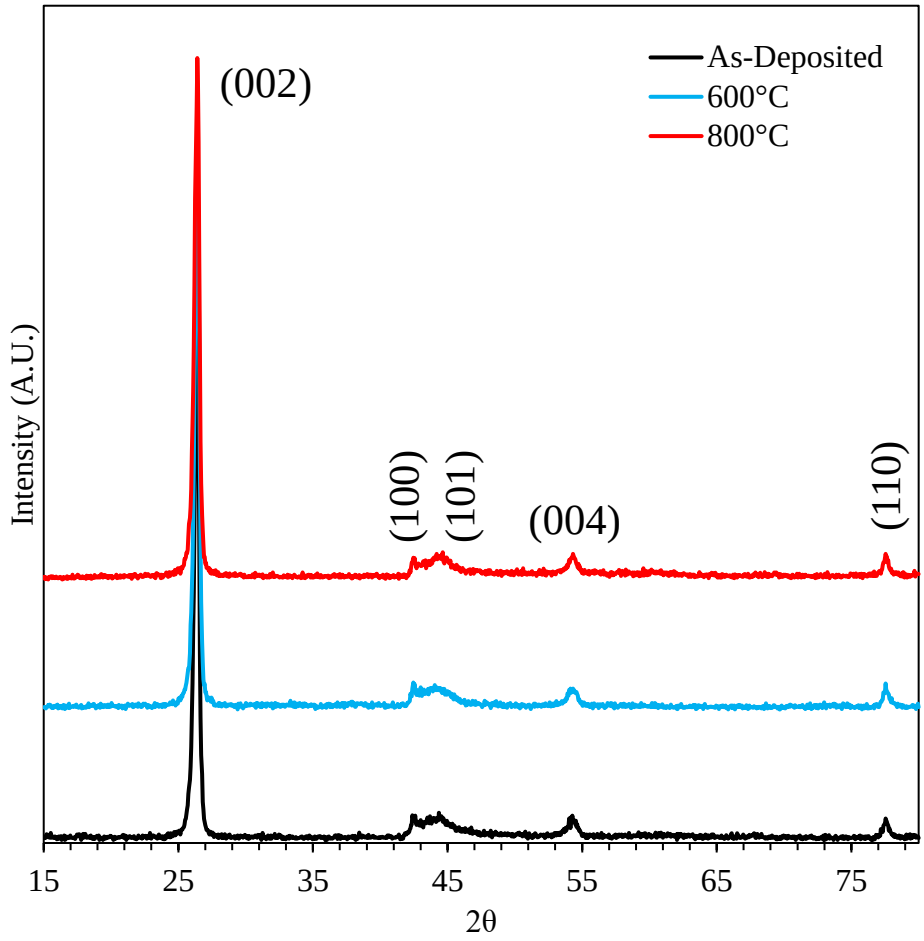

Figure 21. XRD of AXF-5Q + 20nm Ru film in the as-deposited and post-annealed states at 600 and 800°C

A Zeiss Ultra 55 Scanning Electron Microscope (SEM) equipped with energy dispersive spectroscopy (EDS) was utilized to investigate the floor of the crater incurred from SIMS depth profiling. From the typical profile acquired in the graphite collection from SIMS, there exists a sloping tail region disrupting the ideal gaussian behavior and suggests more than one mechanism of diffusion is at play [35]. Figure 22 shows images of the center crater in an IG-110 + Ru sample annealed at 500°C for 24 hours. The brighter regions seen both in and around the crater in

backscattered image in Figure 22B indicate elements with greater atomic weights, with the darker regions belonging to carbon. The depth of the raster area is approximately 800nm deep.

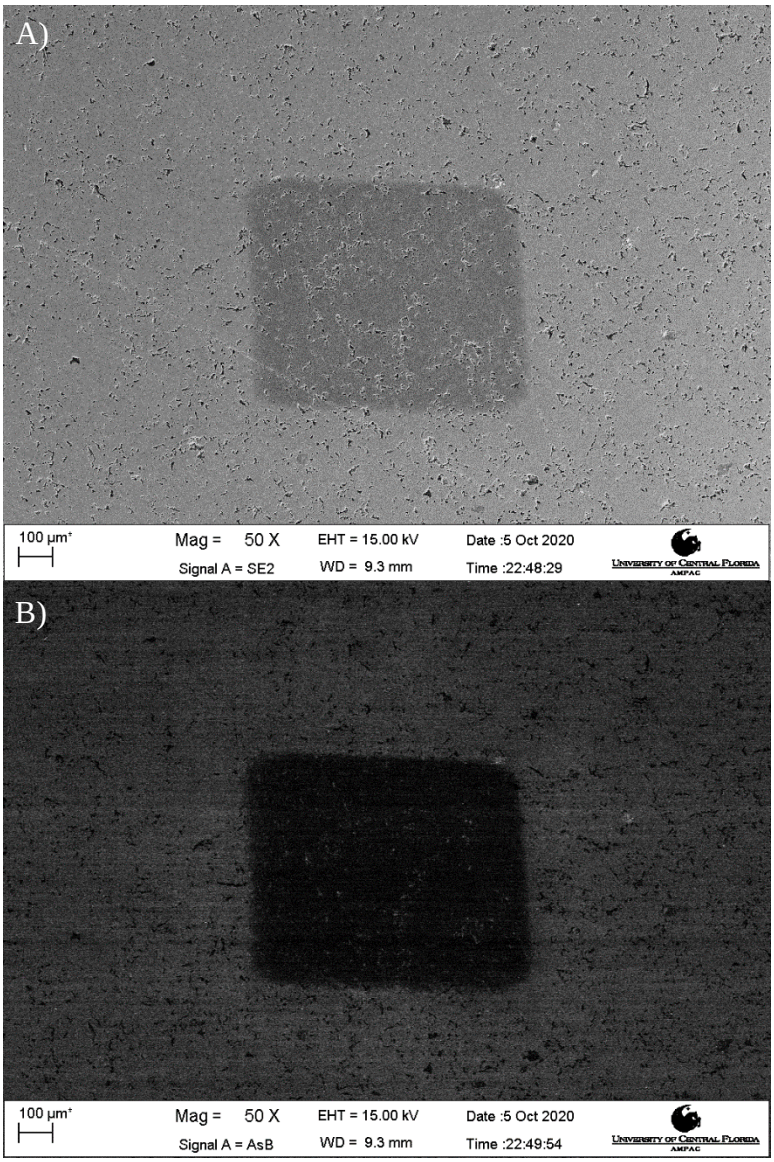

Figure 22. SIMS crater A) secondary electron image, B) backscattered electron image.

Qualitative EDS was carried out at various locations near the center of the crater as this is where ejected particles are collected during SIMS. It can be seen that the heavier elements are

predominately located inside the pores of the graphite structure. Performing points scans on these regions indicates that these highlighted regions are comprised of Ru, Cs or both as shown in C-E in Figure 23. This illustrates that Ru is likely penetrating to greater depths via defects and justifies the inclusion of the short circuit/grain boundary correction equation in the fitting function. Additionally, implantation of the ion source is a common artifact induced by SIMS and is evident in Figure 23D which showcases a region rich in the Cs source material. It too is predominately located in the pores of the bulk material. This could be due to ions impacting inside the pore and implanting or perhaps the ion contains enough energy to sputter but strikes the walls of the pore and remains trapped inside. The small trailing peak beyond the Cs-Lβ1 peak could either be the Cs-Lβ2 peak, the V-Kα peak or the resultant of both peaks with their energies being 4.935keV and 4.952keV respectively [36]. Vanadium is an impurity found in graphite and is not an unexpected occurrence. Figure 23E shows that the dark gray areas are in fact carbon, or plain IG-110 graphite.

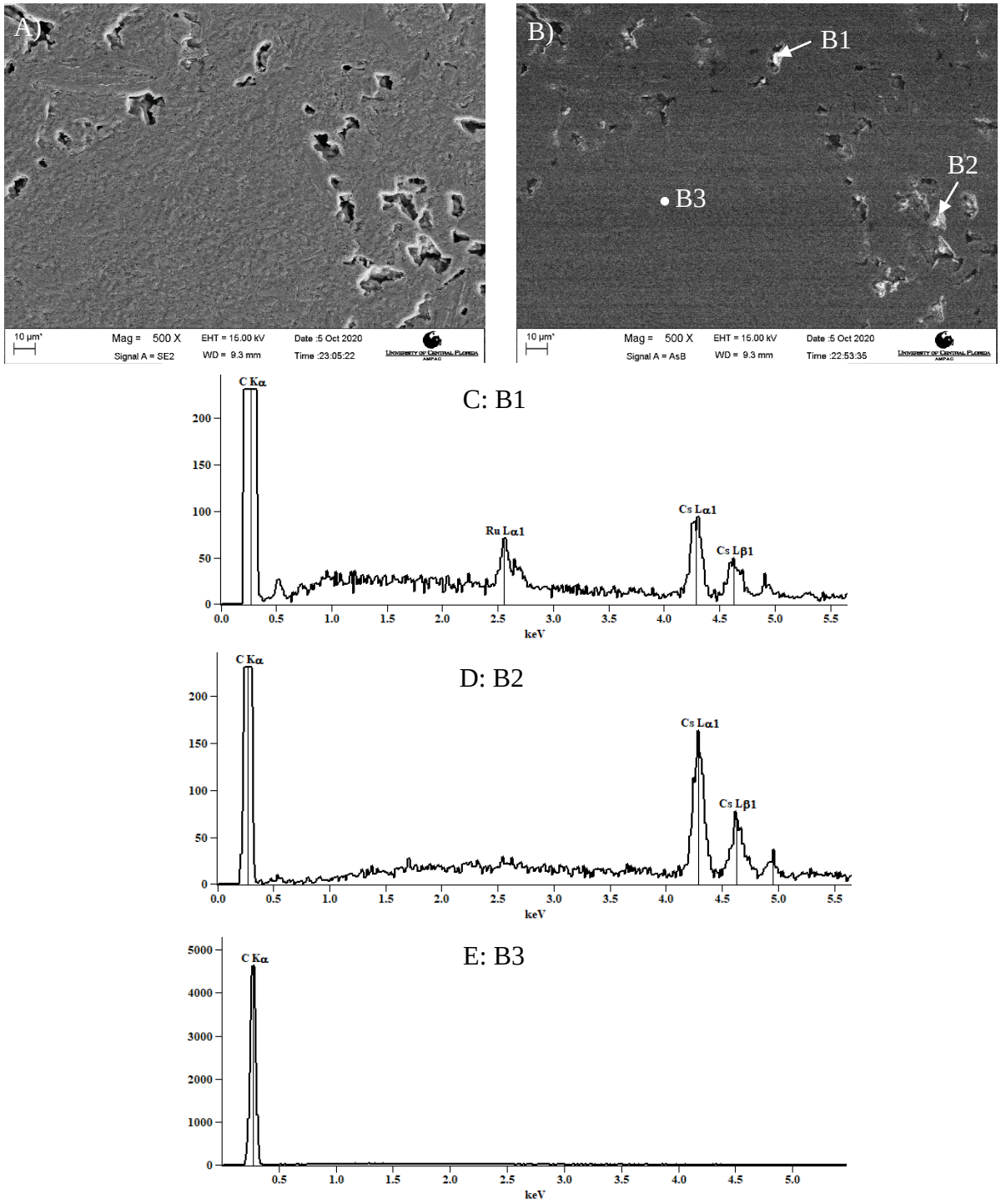

Figure 23. IG-110 + Ru annealed at 500°C, 24hrs. A). Secondary electron image of crater floor. B). Backscattered image of same area. C-E). X-ray counts of points B1-3 respectively.

The center crater of an IG-110 + Ru sample annealed at 800°C for 24 hours also received SEM and EDS treatment. As seen from Figure 24C-E, of the porosities that contain heavier elemental material, ruthenium makes a regular appearance further providing evidence of atomistic travel via grain boundaries. The oxygen peak is expected as oxidation will increase at higher temperatures and graphite oxidizes above 350°C [18]. Additionally, A metal oxide could also have formed between Ru or Cs.

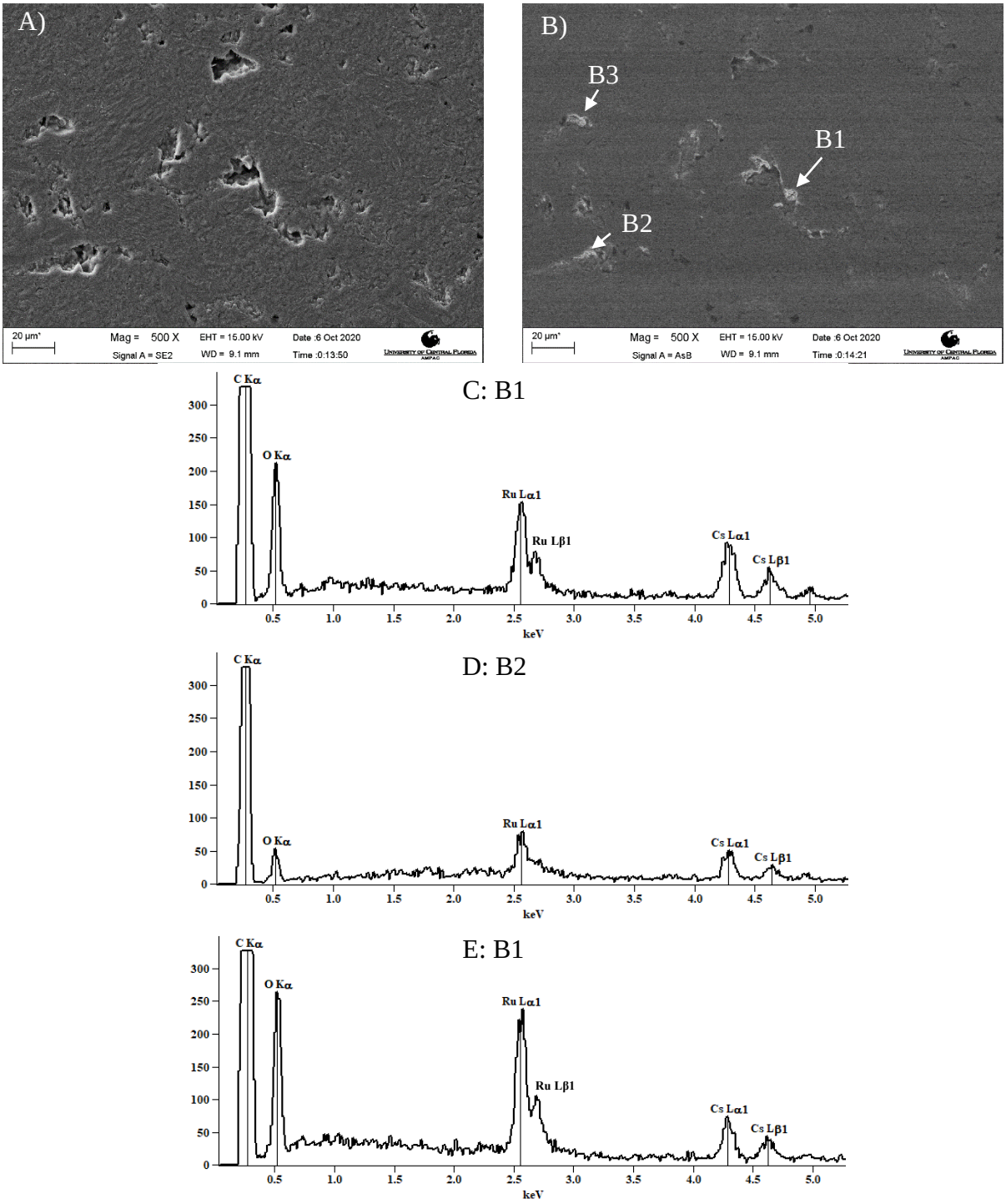

Figure 24. IG-110 + Ru annealed at 800°C, 24hrs. A). Secondary Electron Image. B). Backscattered image of the same region. C-E). Energy spectrum of points B1-3 respectively.

3.5 Discussion

3.5.1 Transport Method

Table 4 shows the derived Arrhenius temperature dependence relations from the experimental diffusion data. While similar activation energies to Ag as reported by Carter *et* al. and others [6, 7, 3] were expected due to both being metal FPs, this was not the case for ruthenium. Activation energies for Ru in each grade were found to be a fraction of those reported for Ag. This is due to the lower temperature dependence of the experimental diffusivity values found in the 500-1000°C temperature range. However, McHugh *et* al [37] recently published simulation work of the adsorption and diffusion of various FPs along a graphene plane. By utilizing the climbing image nudged elastic band method, they calculated the activation energy needed for a Ru particle to travel from one "hollow" region (center of the hexagonal chain) to the next to nearest neighboring hollow region as 0.7449 eV. Travelling to a nearest neighbor site was shown graphically as a lower value of approximately 0.68 eV [37]. Figure 25 depicts this type of movement with the next to nearest neighbor jump being the furthest away. The activation energies determined experimentally in this work are in relatively good agreement with those reported by McHugh *et* al and are shown in Table 5. This indicates that Ru may behave as an intercalating particle travelling along basal planes in the 500-1000°C temperature range.

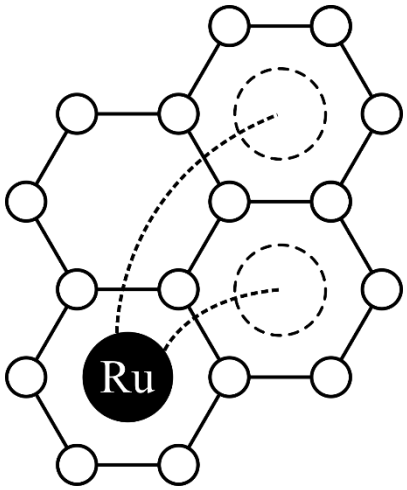

Figure 25. Ru as an intercalating particle moving to neighboring or next to neighboring sites

Table 5. Activation energies of ruthenium in each graphite grade

Graphite Grade	Activation Energy (eV/atom)
AXF-5Q	0.2504
ZXF-5Q	0.2777
IG-110	0.2851
NBG-18	0.4287
PCEA	0.5127

3.5.2 Variability in Calculated Diffusivities

The natural log of the diffusivity typically exhibits linear behavior with the inverse of absolute temperature. Viewing Figure 15Figure 19, the diffusivities found largely do not adhere to linearity, especially those determined at 700°C. Several anneals at a few temperatures were

repeated to judge repeatability and outlier probability. Anneals at 700 and 1000°C for AXF-5Q were repeated to determine if the lower diffusivity behavior was reliably occurring. The resulting values were consistently low for these two temperatures and the average of which were used for the plots in Figure 15 and Figure 20. It can be said then that the behavior at these temperatures is repeatable and not an accidental outlier. Curiously, all grades except ZXF-5Q exhibit this low diffusivity at 700°C and the reason for this behavior is currently unknown but can speculatively by attributed to a Ru clustering at this temperature. Additionally, ZXF-5Q and PCEA may have two different linear regions indicating diffusion occurring by different or additional mechanisms and subsequently different activation energies. For ZXF-5Q in Figure 16, the temperature range of 500-700°C and 800-1000°C exhibit stronger linear behavior but further experimentation at temperatures greater than 1000°C are needed to make that determination. The temperature ranges of 500-600°C and 700-1000°C for PCEA shown in Figure 19 may also be two different profiles. An anneal at 550°C and above 650°C will likely be needed to determine if the trend is true and further investigation will be needed to determine what diffusion mechanism is behind this change.

While the exact cause of the variability in the values acquired is not explicitly known, there are a few factors to consider. Nuclear graphite is manufactured to achieve the highest purity possible however some level of impurity still exists. While the Ru-C phase diagram found in Figure 26 shows immiscibility up until 1940°C, a localized, multicomponent system may be forming between the two constituents of the binary system and an additional impurity at temperatures lower than 1940°C. While this is unlikely due to Ru existing in the matrix at the impurity level, further investigation may be necessary to rule out this possibility [35]. Future characterization efforts on the annealed samples by the project collaborators will likely provide insight on whether other

systems are forming or how the crystal structure is affected by the inclusion of Ru and the inherent impurities.

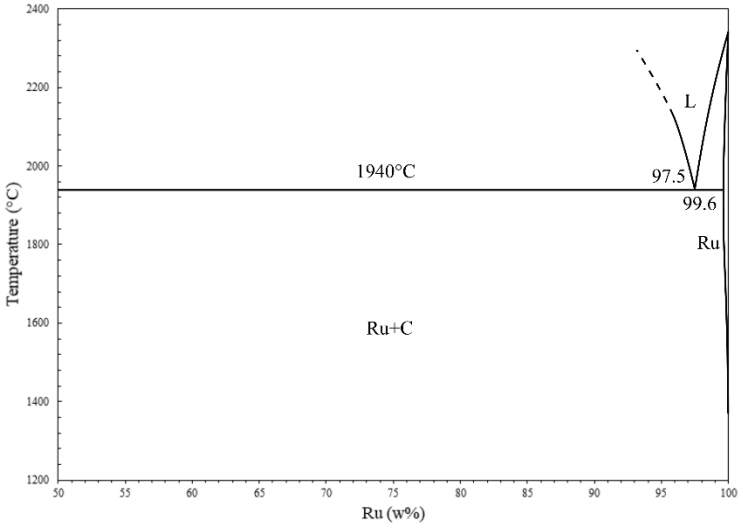

Figure 26. Ru-C phase diagram [38]

SIMS is a highly sensitive analysis technique. However, as with any analysis method, there are certain artifacts that can occur. One such defect is atomic mixing. The primary ions may not induce sputtering of the atoms on the surface and instead push them deeper into the sample. This can result in greater counts for a species at a larger depth and thus not accurately represent the sample. This was realized upon depth profiling with an oxygen source on as-deposited samples when extended depths of film thicknesses were captured due to poor sputtering ability. Cs^+ ions were made the primary source and better sputtering was achieved however some pushing is still expected to exist. In addition, molecules may be sputtered off and contain the same mass as other species in the sample. For example, Ru and V have an atomic mass of 101.1 and 50.94 respectively. two vanadium particles nearly equal the mass of one ruthenium particle which can lead to false

ruthenium counts if the mass spectrometer is not able to correctly resolve the two different masses. This has been captured in a couple of profiles as increased background. These depth profiles were excluded in the diffusivity calculations but the possibility of scattered V impurities still remains.

In an attempt to determine if there was error on the deposition and annealing side of this work that may lead to variability in the data, several tests were performed. Furnace temperature testing with external type S thermocouples were employed as an independent accuracy check of the set point temperature for all furnaces used. Temperature data was collected over a 24-hour period and the furnaces were accurate to ±3°C. Uniformity of the deposited metal film was also investigated. Small pieces of sapphire were placed at varying radiuses starting from the center and extending to near the edge of the plate. 20nm of ruthenium was deposited using the same parameters and procedure as the previous Ru depositions. Figure 27 shows the sapphire post-deposition. X-ray reflectivity was used to measure film thickness which resulted in a thickness of 20.84 ± 0.14nm. From this test, it is concluded that sample thickness is consistent and independent of location during FP depositions.

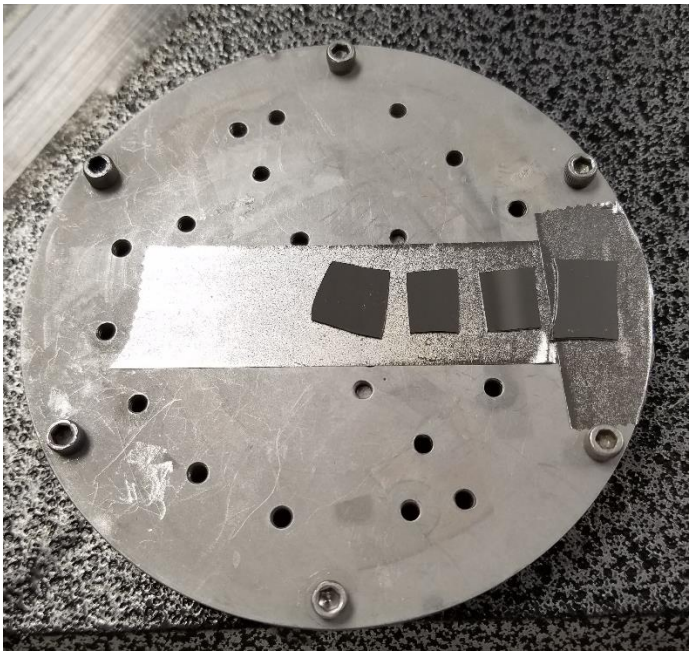

Figure 27. Film thickness by location testing, post deposition

3.6 Summary

Through the use of PVD, SIMS and thin film analysis of acquired depth profiles, the diffusivities and their Arrhenius behavior of ruthenium in AXF-5Q, ZXF-5Q, NBG-18, IG-110 and PCEA graphite in a temperature range of 500-1000°C have been found. These previously unreported values start the discussion of the transport of the FP ruthenium in the five grades considered for the next generation of nuclear reactors. From the SIMS depth profiles, non-gaussian behavior was observed due to an extended tail region that could be from the influence of grain boundary diffusion. Initial characterization work was carried out by SEM coupled with EDS and ruthenium was found to reside in the defects at the bottom of the SIMS crater, confirming short circuit diffusion was occurring and justifying the use of the additional term to fit the depth profiles. A standardized methodology was developed by fitting from the inflection point of the depth profile

to avoid any non-steady state sputtering and surface effects from SIMS. This allowed for the bulk diffusivity values to be back calculated from the profiles after numerical fitting. Some unexpected diffusivity values were found, namely at 700°C. Experiments at this temperature were repeated for AXF-5Q and the behavior was found to be consistent. Further analysis will be needed to explain the phenomena behind this result. While there is some departure from linearity in the determined diffusivity values, Arrhenius equations valid for the range of 500-1000°C have been reported for the first time for ruthenium in these grades. The activation energies found by simulation for a ruthenium atom traversing a graphene plane has relatively good agreement with the activation energies found for ruthenium diffusing through the graphite grades studied in this work. It can then be said that Ru exists in the graphite as an intercalating atom and uses the spacing between graphene-like basal layers as a transport method through the matrix.

LIST OF REFERENCES

[1] P. Breeze, "Nuclear Power," in *Power Generation Technologies*, Newnes, 2019, pp. 399-429.

[2] L. M. Carter, J. D. Brockman, J. D. Robertson and S. K. Loyalka, "Diffusion of cesium and iodine in compressed IG-110 graphite compacts," *Journal of Nuclear Materials,* vol. 476, pp. 30-35, 2016.

[3] International Atomic Energy Agency, "Fuel performance and fission product behaviour in gas cooled reactors," 1997.

[4] T. R. Boyle, R. V. Tompson, S. K. Loyalka, T. K. Ghosh and M. L. Reinig Jr., "Measurement of Silver Diffusion in VHTR Graphitic Materials," *Nuclear Technology,* vol. 183, no. 2, pp. 149-159, 2013.

[5] F. F. Zherdev and P. A. Platonov, "Diffusion of the fission metals cesium and silver in reactor-grade graphite," *Journal of Nuclear Materials,* no. 182, pp. 223-229, 1991.

[6] L. M. Carter, J. D. Seelig, J. D. Brockman, J. D. Robertson and S. K. Loyalka, "ICP-MS measurement of silver diffusion coefficient in graphite IG-110 between 1048K and 1284K," *Journal of Nuclear Materials,* vol. 498, no. January, pp. 44-49, 2018.

[7] E. Hoinkis, "The diffusion of silver in the graphitic matrices A3-3 and A3-27," *Jounral of Nuclear Materials,* vol. 209, no. 2, pp. 132-147, 1994.

[8] International Atomic Energy Agency, "Open Knowledge Wiki - Fundamentals of Nuclear Power," [Online]. Available: https://nucleus.iaea.org/sites/graphiteknowledgebase/wiki/Guide_to_Graphite/Fundamentals%20of%20Nuclear%20Power.aspx.

[9] Nuclear Reactor Laboratory: Massachusetts Institute of Technology, "The Fission Process," Nuclear Reactor Laboratory, 2018. [Online]. Available: https://nrl.mit.edu/reactor/fission-process.

[10] National Institute of Standards and Technology, "Neutron scattering lengths and cross sections," 2013. [Online]. Available: https://www.ncnr.nist.gov/resources/n-lengths/elements/c.html.

[11] A. Kamal, "Nuclear Reactions," in *Nuclear Physics*, Berlin Heidelberg, Springer Berlin Heidelberg, 2014, pp. 425-502.

[12] Generation IV International Forum, "Very-High-Temperature-Reactor," [Online]. Available: https://www.gen-4.org/gif/jcms/c_42153/very-high-temperature-reactor-vhtr.

[13] Z. Wu, D. Lin and D. Zhong, "The design features of the HTR-10," *Nuclear Engineering and Design*, vol. 218, no. 1-3, pp. 25-32, 2002.

[14] S. Shiozawa, S. Fujikawa, T. Iyoku, K. Kunitomi and Y. Tachibana, "Overview of HTTR design features," *Nuclear Engineering and Design*, vol. 233, no. 1-3, pp. 11-21, 2004.

[15] Office of Nuclear Energy, "TRISO Particles," Office of Nuclear Energy, [Online]. Available: https://www.energy.gov/ne/articles/triso-particles-most-robust-nuclear-fuel-earth.

[16] B. J. Marsden, A. N. Jones, G. N. Hall and P. M. Mummery, "14 - Graphite as a core material for Generation IV nuclear reactors," in *Structural Materials for Generation IV Nuclear Reactors*, Duxford, Woodhead Publishing, 2017, pp. 495-532.

[17] R. E. Nightingale, Nuclear Graphite, New York: Academic Press, 1962.

[18] POCO Graphite, "Properties and Characteristics of Graphite," January 2015. [Online]. Available: https://www.entegris.com/content/dam/web/resources/manuals-and-guides/manual-properties-and-characteristics-of-graphite-109441.pdf.

[19] ASTM International, "D7219-19 Standard Specification for Isotropic and Near-isotropic Nuclear Graphites," West Conshohocken, PA, 2019.

[20] National Cancer Institute, "Coal Tar and Coal-Tar Pitch," 28 December 2018. [Online]. Available: https://www.cancer.gov/about-cancer/causes-prevention/risk/substances/coal-tar.

[21] E. Fitzer, K. -H. Kochling, H. P. Boehm and H. Marsh, "Recommened Terminology for the description of carbon as a solid (IUPAC Recommendations 1995)," *Pure and Applied Chemistry*, vol. 67, no. 3, pp. 473-506, 1995.

[22] G. Vasudevamurthy, T. S. Byun, P. Pappano, L. L. Snead and T. D. Burchell, "Effect of specimen size and grain orientation on the mechanical and physical properties of NBG-18 nuclear graphite," *Journal of Nuclear Materials,* vol. 462, pp. 1-7, 2015.

[23] X. Luo, J.-C. Robin and S. Yu, "Comparison of Oxidation Behaviors of Different Grades of Nuclear Graphite," *Nuclear Science and Engineering,* vol. 151, no. 1, pp. 121-127, 2005.

[24] W.-t. Zhang, B.-l. Zhang, J.-l. Song, W. Qi, X.-j. He, Z.-j. Liu, P.-f. Lian, Z.-t. He, L.-n. Gao, H.-h. Xia, X.-d. Liu, X.-t. Zhou, L.-b. Sun and X.-x. Wu, "Microstructure and molten salt impregnation characteristics of a micro-fine grain graphite for use in molten salt reactors," *New Carbon Materials,* vol. 31, no. 6, pp. 585-593, 2016.

[25] M. S. El-Genk and J.-M. P. Tournier, "Comparison of oxidation model predictions with gasification data of IG-110,IG-430 and NBG-25 nuclear graphite," *Journal of Nuclear Materials,* vol. 420, no. 1-3, pp. 141-158, 2012.

[26] J. Kane, C. Karthik, D. P. Butt, W. E. Windes and R. Ubic, "Microstructural characterization and pore structure analysis of nuclear graphite," *Journal of Nuclear Materials,* vol. 415, no. 2, pp. 189-197, 2011.

[27] Entegris, "Types of Properties of Industrial Graphite Grades," 2020. [Online]. Available: https://poco.entegris.com/content/dam/poco/shared-product-assets/industrial-grades/specsheet-industrial-table.pdf. [Accessed 18 September 2020].

[28] T. Burchell, R. Bratton and W. Windes, "NGNP Graphite Selection and Acquisition Strategy," Oak Ridge National Laboratory, Oak Ridge, 2007.

[29] P. Beghein, G. Berlioux, B. d. Mesnildot, F. Hiltmann and M. Melin, "NBG-17 – An improved graphite grade for HTRs and VHTRs," *Nuclear Engineering and Design*, vol. 251, no. October, pp. 146-149, 2012.

[30] S. Hofmann, "Sputter depth profile analysis of interfaces," *Reports on Progress in Physics*, vol. 61, no. 7, pp. 827-888, 1998.

[31] J. E. Baker, "Secondary Ion Mass Spectrometry," in *Practical Materials Characterization*, New York, Springer, 2014, pp. 133-187.

[32] D. S. McPhail, "Applications of Secondary Ion Mass Spectrometry (SIMS) in Materials Science," *Journal of Materials Science*, no. 41, pp. 873-903, 2006.

[33] H. Mehrer, Diffusion in Solids: Fundamentals, Methods, Materials, Diffusion-Controlled Processes, Berlin: Springer, 2007.

[34] J. T. McClave and F. H. Dietrich, II, in *Statistics*, San Francisco, Dellen Publishing Company, 1988, pp. 683-737.

[35] A. Paul, T. Laurila, V. Vuorinen and S. V. Divinski, Thermodynamics, Diffusion and the Kirkendall Effect in Solids, Springer , 2014.

[36] EDAX, "EDAX Peak Identification Chart".

[37] J. G. McHugh, K. Jolley and P. Mouratidis, "Ab-initio calculations of fission product diffusion on graphene," *Journal of Nuclear Materials,* vol. 533, no. May 2020.

[38] ASM International, Binary Alloy Phase Diagrams, 2nd Edition, ASM International, 1990.